



**HAL**  
open science

# A first look at Ge/Si partitioning during amorphous silica precipitation: Implications for Ge/Si as a tracer of fluid-silicate interactions

Nicole M. Fernandez, Alida Perez-Fodich, Louis A. Derry, Jennifer L. Druhan

## ► To cite this version:

Nicole M. Fernandez, Alida Perez-Fodich, Louis A. Derry, Jennifer L. Druhan. A first look at Ge/Si partitioning during amorphous silica precipitation: Implications for Ge/Si as a tracer of fluid-silicate interactions. *Geochimica et Cosmochimica Acta*, 2021, 297, pp.158-178. 10.1016/j.gca.2021.01.007 . insu-03590083

**HAL Id: insu-03590083**

**<https://insu.hal.science/insu-03590083>**

Submitted on 13 Feb 2023

**HAL** is a multi-disciplinary open access archive for the deposit and dissemination of scientific research documents, whether they are published or not. The documents may come from teaching and research institutions in France or abroad, or from public or private research centers.

L'archive ouverte pluridisciplinaire **HAL**, est destinée au dépôt et à la diffusion de documents scientifiques de niveau recherche, publiés ou non, émanant des établissements d'enseignement et de recherche français ou étrangers, des laboratoires publics ou privés.



Distributed under a Creative Commons Attribution - NonCommercial 4.0 International License

1 **A first look at Ge/Si partitioning during amorphous silica precipitation: Implications for**  
2 **Ge/Si as a tracer of fluid-silicate interactions**

3  
4 Nicole M. Fernandez<sup>1,2\*</sup>, Alida Perez-Fodich<sup>3</sup>, Louis A. Derry<sup>2,4</sup>, Jennifer L. Druhan<sup>1</sup>

5  
6 <sup>1</sup>Department of Geology, University of Illinois at Urbana Champaign, Urbana, IL 61801 USA

7 <sup>2</sup>Université de Paris, Institut de Physique du Globe de Paris, CNRS, F-75005 Paris, FR

8 <sup>3</sup>Department of Geology, University of Chile, Santiago, Chile

9 <sup>4</sup>Department of Earth Science, Cornell University, Ithaca, NY 14853 USA

10 Corresponding author email: [n.fernandez@cornell.edu](mailto:n.fernandez@cornell.edu)

11 **ABSTRACT**

12 We measured germanium-silicon (Ge/Si) ratios in both fluid and solid phases using a  
13 series of highly constrained amorphous silica precipitation experiments at 20°C and neutral  
14 pH for a wide range of seed crystal surface areas. Silicon isotope data ( $\delta^{30/28}\text{Si}$ ) on these  
15 experiments were previously reported by Fernandez et al. (2019). A distinct lag in the onset of  
16 Ge/Si partitioning relative to  $\delta^{30}\text{Si}$  fractionation during active amorphous silica growth  
17 indicated that Ge incorporation rates were orders of magnitude slower than silicon  
18 precipitation rates. Slow Ge kinetics give the appearance of conservative behavior over short  
19 experimental timescales (~30 days). A major outcome from these observations was the  
20 existence of distinct equilibration timescales between Ge/Si and  $\delta^{30}\text{Si}$ . Further, these  
21 experimental results provide the first documented evidence of rate dependent behavior in Ge  
22 partition coefficients. Successful application of a modified solid solution model, initially  
23 developed for characterizing stable isotope fractionation, indicates that a common  
24 fractionation model theory is able to describe both Ge/Si and  $\delta^{30}\text{Si}$  partitioning. Numerical  
25 simulations conducted at longer timescales (1 to 1000 years) predict eventual Ge  
26 incorporation into the mineral surface, but this occurs when the system is in close proximity  
27 to equilibrium conditions. These long-term predictions underscore the potential of Ge as a

28 (near)equilibrium tracer in complement to the mixed kinetic and equilibrium signatures  
29 recorded by  $\delta^{30}\text{Si}$ . Our findings illustrate the viability of a combined Ge/Si– $\delta^{30}\text{Si}$  multi-tracer  
30 approach for constraining silicate mineral formation across a variety of terrestrial and marine  
31 systems.

32

## 33 1. INTRODUCTION

34 Shared characteristics between trace element Germanium (Ge) and major element Silicon  
35 (Si) make germanium to silicon (Ge/Si) ratios valuable tracers of the global silicon cycle  
36 (Mortlock and Froelich, 1987; Murnane and Stallard, 1990; Froelich et al., 1985, 1992;  
37 Hammond et al., 2000; King et al., 2000; Kurtz et al., 2002; Derry et al., 2005; Baronas et al.,  
38 2018). Ge and Si are both group IV elements and have similar electronic configurations as  
39 both reside within the ‘p-block’ of the periodic table. They have similar oxygen bond lengths  
40 (Si–O and Ge–O are 1.75 and 1.64 Å, respectively) and are of similar sizes, where Ge is  
41 slightly larger (atomic radius = 0.53 Å) compared to Si (atomic radius = 0.41 Å). These  
42 common atomic properties facilitate the incorporation of Ge into secondary silicate phases as  
43 a substitute for Si in the same manner commonly observed for other pseudo-isotope trace  
44 replacements, such as Sr for Ca in carbonates, following Goldschmidt’s principle  
45 (Goldschmidt, 1926, 1958). In this respect Ge can be considered as a pseudo-isotope of  
46 silicon, imitating Si behavior across the biogeochemical Si cycle from the chemical  
47 weathering of rocks to the uptake of diatoms in the oceans and throughout long-term storage  
48 as deep marine sediments. Like the silicon stable isotope ( $\delta^{30}\text{Si}$ ) tracer, Ge/Si ratios are  
49 partitioned due to a distinct subset of biogeochemical processes, notably secondary mineral  
50 formation, biological uptake, and adsorption onto Fe-(hydr)oxides. These pathways cause Ge  
51 to partition from Si based on compatibility and substitution mechanisms just as they invoke  
52 mass dependent fractionations between heavy  $^{30}\text{Si}$  and light  $^{28}\text{Si}$  isotopes (Opfergelt et al.,

53 2010; Delvigne et al., 2016; Baronas et al., 2018). The magnitude of partitioning between the  
54 reacting phases (i.e., fluid and solids) for Ge/Si is generally characterized by a partition  
55 coefficient  $\left(K_D = \frac{Ge/Si\ product}{Ge/Si\ reactant}\right)$ . This is comparable to  $\delta^{30}Si$  fractionation, described by a  
56 fractionation factor  $\left(\alpha = \frac{R_{product}}{R_{reactant}}\right)$  where  $R = \frac{^{30}Si}{^{28}Si}$ .

57 In natural environments, congruent mineral dissolution is not associated with any  
58 systematic  $\delta^{30}Si$  or Ge/Si fractionation (Wada and Wada, 1982; Kurtz et al., 2002). Abiotic  
59 silicate mineral precipitation is a major fractionating pathway for both  $\delta^{30}Si$  (Ziegler et al.,  
60 2005a,b; Georg et al., 2006, 2007, 2009; Opfergelt et al., 2012; Pogge von Strandmann et al.,  
61 2012; Hughes et al., 2013; Riotte et al., 2018; and others) and Ge/Si (Kurtz et al., 2002;  
62 Scribner et al., 2006; Lugolobi et al., 2010; Aguirre et al., 2017; Ameijeiras-Marino et al.,  
63 2018; Qi et al., 2019; Perez-Fodich and Derry, 2020). This process distinguishes the  
64 compositions of the forming solid phase and surrounding fluid as a function of the rate and  
65 extent of mineral growth.

66 Ge/Si and  $\delta^{30}Si$  have been shown to co-evolve under terrestrial weathering conditions  
67 (Lugolobi et al., 2010; Opfergelt et al., 2010; Delvigne et al., 2016; Baronas et al., 2018,  
68 2020) and, for the most part, the manner in which they fractionate is thought to be  
69 comparable. For secondary clays,  $\delta^{30}Si$  and Ge/Si signatures are typically inversely correlated  
70 in that the light  $^{28}Si$  is preferentially incorporated into the newly-formed clay due to kinetic  
71 isotope effects and Ge is similarly preferentially partitioned into the solid phase as a result of  
72 compatibility with secondary clays at equilibrium ( $K_d \sim 10.7$  on average for secondary clays;  
73 Kurtz et al., 2002). The result is a secondary clay low in  $\delta^{30}Si$ , ranging from -2.95 to -0.16 ‰  
74 (Ziegler et al., 2005a,b; Georg et al., 2006; Cornelis et al., 2010; Opfergelt et al., 2012;  
75 Hughes et al., 2013. Frings et al., 2016; Riotte et al., 2018; and others) and elevated in Ge/Si,  
76 reaching values greater than  $5\ \mu\text{mol mol}^{-1}$  (Kurtz et al., 2002; Lugolobi et al., 2010; Opfergelt

77 et al., 2010; Aguirre et al., 2017; Ameijeiras-Marino et al., 2018; Qi et al., 2019). Thus, the  
78 fluid from which these mineral phases form must become isotopically heavier (i.e., higher  
79  $\delta^{30}\text{Si}$  values) and lower in Ge/Si with respect to the bedrock or minerals which were originally  
80 solubilized.

81 Some circumstances cause distinct  $\delta^{30}\text{Si}$  and Ge/Si behavior. Notably,  $\delta^{30}\text{Si}$  and Ge/Si are  
82 decoupled from one another during uptake by vascular plants, where light  $^{28}\text{Si}$  is  
83 preferentially incorporated into the phytoliths while Ge is generally excluded. This results in  
84 high soil water Ge/Si and  $\delta^{30}\text{Si}$  and correspondingly lower values in phytoliths (Blecker et al.,  
85 2007; Derry et al., 2005; Meek et al., 2016). Despite these noted exceptions, we generally  
86 anticipate that the underlying fractionation mechanisms for  $\delta^{30}\text{Si}$  and Ge/Si are inherently  
87 analogous during mineral neof ormation (similar to that proposed for Ca stable isotopes and  
88 Sr/Ca ratios; DePaolo, 2011). However, despite numerous examples of  $\delta^{30}\text{Si}$  and Ge/Si co-  
89 evolution in the field, the behavior of these two tracers during secondary silicate precipitation  
90 has yet to be directly demonstrated.

91 To explore the extent to which  $\delta^{30}\text{Si}$  and Ge/Si fractionation are influenced by both  
92 kinetic and equilibrium effects, including the potential for co-evolution of the mineral surface  
93 and fluid in the transition from kinetically controlled to near-equilibrium conditions, we  
94 analyzed samples from a series of highly constrained amorphous silica precipitation  
95 experiments recently reported by Fernandez et al. (2019). This approach leveraged the  
96 relatively rapid kinetics of amorphous silica formation (Geilert et al., 2014; Roerdink et al.,  
97 2015) to document  $\delta^{30}\text{Si}$  fractionation behavior under variable or “free-drifting” conditions  
98 (i.e., where saturation states and solute compositions are allowed to change with reaction  
99 progress) across a range of seed crystal specific surface areas (e.g., a range of growth rates)  
100 and solid to fluid ratios. The study showed clear evidence for kinetic isotope fractionation  
101 followed by rapid isotopic re-equilibration as a function of the overall precipitation rate and,

102 thus, by extension the surface area of seeds used in the experiments. In this context, the  
103 mechanisms of  $\delta^{30}\text{Si}$  fractionation during amorphous silica precipitation were comparable to  
104 that of  $\delta^{44}\text{Ca}$  during carbonate formation (Tang et al., 2008; DePaolo 2011). But, due to the  
105 free drift nature of the experiments, these data were shown to depend on both chemical  
106 (saturation state, solute compositions) and physical (surface area, solid to fluid ratio)  
107 characteristics of the system. Thus, the utility of the silicon isotopic tracer incorporates a  
108 variety of physiochemical effects and parsing this signature in natural settings could pose a  
109 poorly constrained problem if and when all factors are varying.

110 Viewed in this way, the analogous behavior of Ge/Si ratios offer a promising tool to  
111 complement  $\delta^{30}\text{Si}$  if the factors affecting this signature can be similarly constrained within a  
112 unified model framework. To test whether  $\delta^{30}\text{Si}$  and Ge/Si follow analogous fractionation  
113 pathways for amorphous silica formation, we applied a numerical multi-component  
114 geochemical model adapted from the principles of the SRKM (surface reaction kinetic model)  
115 proposed by DePaolo (2011) to our “free-drift” experimental data. This model framework has  
116 been successfully used in the past to describe  $\delta^{44}\text{Ca}$  and Sr/Ca fractionation in calcite  
117 precipitation experiments (Tang et al., 2008; AlKhatib and Eisenhauer, 2018) and has been  
118 recently applied to describe  $\delta^{30}\text{Si}$  fractionation during amorphous silica formation (Roerdink  
119 et al., 2015; Fernandez et al., 2019).

120 This study reports the first direct documentation of the extent of Ge incorporation and  
121 Ge/Si fractionation during active amorphous silica precipitation under highly constrained  
122 laboratory conditions. This experiment is the first, to our knowledge, to directly parse the  
123 effects of kinetically limited mineral growth on Ge/Si relative to  $\delta^{30}\text{Si}$  signatures. Our  
124 findings have direct implications for interpretation of Ge/Si ratios observed in a variety of  
125 field settings where amorphous silica precipitation exerts a large control on silicon

126 (bio)geochemical cycling. Examples include silicate weathering in the critical zone,  
127 hydro(geo)thermal activity, and marine diagenesis and recrystallization.

## 128 2. METHODS

### 129 2.1 Batch experiments

130 The samples analyzed in this study were generated from amorphous silica precipitation  
131 batch experiments reported in Fernandez et al. (2019). We refer the reader to this prior  
132 publication for complete descriptions of the experimental design and initial conditions. To  
133 summarize, amorphous silica precipitation experiments were conducted in three closed batch  
134 reactors each with a different set of  $\text{SiO}_{2(s)}$  seed crystal surface areas and solid to fluid silicon  
135 mass ratios (50 to 31  $\text{SiO}_{2(s)}$  [g]: $\text{SiO}_{2(aq)}$ [g]) at an ambient temperature of 20°C. All  
136 experiments started at a comparable dissolved  $\text{SiO}_{2(aq)}$  concentration (5.3 mM) and pH (7.3)  
137 and were run for approximately 30 days, resulting in an initial oversaturation of  $0.48 \pm 0.06$   
138 ( $\log Q/K$ ) with respect to  $\text{SiO}_{2(s)}$ . Each batch reactor contained one of three seed crystal grain  
139 sizes, with specific surface areas that will from now on be referred to as high ( $\text{SSA} = 50 \text{ m}^2 \text{ g}^{-1}$ )  
140  $^1$ ), medium ( $\text{SSA} = 0.127 \text{ m}^2 \text{ g}^{-1}$ ), and low ( $\text{SSA} = 0.072 \text{ m}^2 \text{ g}^{-1}$ ) experiments. Initial seed  
141 Ge/Si ratios for the high, medium, and low surface area grains were  $0.28 \pm 0.01 \mu\text{mol mol}^{-1}$ ,  
142  $0.56 \pm 0.02 \mu\text{mol mol}^{-1}$ , and  $0.64 \pm 0.02 \mu\text{mol mol}^{-1}$ , respectively. Starting oversaturated  
143 solutions were prepared by dissolving 10 g of high surface area fumed silica grains in 1L of  
144 MQ-e water at 90°C for ~1 week until starting  $\text{SiO}_{2(aq)}$  concentration were reached. Ge was  
145 introduced through leaching via the dissolution of these high surface area seeds ( $\text{Ge/Si} = 0.28$   
146  $\pm 0.01 \mu\text{mol mol}^{-1}$ ) at 90°C, resulting in a starting Ge:Si content in the fluid of  $0.044 \pm 0.002$   
147  $\mu\text{M} : 0.00530 \pm 0.00003 \text{ M}$  (initial fluid Ge/Si ratio =  $\sim 8.45 \pm 0.3 \mu\text{mol mol}^{-1}$ ). The difference  
148 in seed crystal and starting solution Ge/Si ratios is discussed further in **section 4.1**.

149 The next steps in the preparation of the starting solution followed different protocols  
150 depending on the type of surface area seeds used in each batch. For the batch involving high

151 surface area seeds, the starting solution after the pre-dissolution step at 90°C was cooled  
152 directly to 20°C. In the medium and low surface area batches, the starting solutions were  
153 subjected to vacuum filtration to remove the undissolved high surface area grains and  
154 subsequently cooled to 20°C. In all batches, initially acidic solutions (pH ~ 4.5) were then  
155 titrated with 10 mM NaOH to the target starting pH (7.3). This increase in pH to near-neutral  
156 values was sufficient to initiate precipitation in the high surface area case. For the low and  
157 medium surface area cases, amorphous silica seed crystals of appropriate size were also added  
158 in order to start the reaction. In all batches, precipitation occurred onto pre-existing grains  
159 homogeneously distributed in solution with starting masses of approximately 4 g for the  
160 medium and low surface area batches and 0.5 g for the high surface area batch. Experiments  
161 were run for a duration of ~30 days while being continuously agitated on a shaker plate.  
162 Samples were withdrawn at regular time intervals in aliquots of 2.5mL using a disposable  
163 syringe and 0.22µm nylon filter. A fraction of the sample (2 mL) was subsequently diluted to  
164 10 mL with ultrapure water in preparation for silicon stable isotope and Ge concentration  
165 analyses. Experiments were terminated after the last sample was taken and amorphous silica  
166 grains were separated out of the remaining solution via vacuum filtration. Initial experimental  
167 conditions across all seed crystal surface areas are reported in **Table 1**.

## 168 **2.2 Germanium analyses**

169 Germanium concentrations were analyzed using hydride-generation ICP mass-  
170 spectrometry (HG-ICP-MS) (Mortlock & Froelich, 1996; Aguirre et al. 2017) at Cornell  
171 University with a custom HG sample introduction system and a Thermo-Finnigan Element 2  
172 ICP-MS. Aqueous samples were prepared by adding an enriched <sup>70</sup>Ge spike solution and  
173 allowed to equilibrate for at least 48 hours at room temperature. The spike solution was added  
174 to target a <sup>70</sup>Ge/<sup>74</sup>Ge ratio of 10, estimated from the Si concentrations. To measure Ge  
175 concentrations, the prepared samples were introduced into the hydride generation system with

176 a 4% NaBH<sub>4</sub> solution to reduce aqueous Ge(OH)<sub>4</sub> to volatile GeH<sub>4</sub>, passing through an gas-  
177 liquid-separation filter along with Ar as carrier gas into the ICP-MS. Germanium was  
178 quantified by isotope dilution using the <sup>70</sup>Ge/<sup>74</sup>Ge ratio. Mass bias and signal drift were  
179 corrected using standard sample bracketing. We measured Ge standards at 5, 20, 50, 100 and  
180 200 ng L<sup>-1</sup>. To cross-check the isotope dilution calculations, standard response curves were  
181 generated at m/z =74 for each Ge concentration. The <sup>70</sup>Ge/<sup>74</sup>Ge in the spike is equal to 162,  
182 thus the contribution from the spike at m/z = 74 is insignificant. Analytical uncertainty for  
183 these measurements is approximately 3% RSD (Kurtz et al., 2002; Derry et al., 2005;  
184 Lugolobi et al., 2010; Kurtz et al., 2011). The contribution of the spike addition to the  
185 uncertainty of Ge measurements is negligible (Heumann, 1988).

### 186 **2.3 Model design and assumptions**

187 Ge partitioning during amorphous silica precipitation was simulated using the multi-  
188 component reactive transport software, CrunchTope (Steeffel et al., 2015). The fractionation  
189 model framework within CrunchTope uses a two-endmember solid solution (Druhan et al.,  
190 2013) to create a simple, binary mechanical mixture between two substituting elements in a  
191 solid phase such as rare and major isotopes of a major element (ex. <sup>28</sup>Si<sub>1-x</sub><sup>30</sup>Si<sub>x</sub>O<sub>2(am)</sub>) or trace  
192 and major elements (ex. Si<sub>1-x</sub>Ge<sub>x</sub>O<sub>2(am)</sub>), where *x* represents the mole fraction of either the rare  
193 isotope or trace element. For the purposes of the current study, an ideal solid solution  
194 between amorphous GeO<sub>2</sub> and SiO<sub>2</sub> takes the following form (Eq. 1):



196 where Ge in the form of Ge(OH)<sub>4(aq)</sub> species in solution is shown substituting for Si in  
197 amorphous silica, SiO<sub>2(am)</sub>, in this solid solution stoichiometry and *x* represents the mole  
198 fraction of GeO<sub>2(am)</sub>. In an ideal solid solution each element (in the case of isotopes, each  
199 individual isotope), can substitute for one another in the same site within the crystal structure  
200 with negligible changes to the thermodynamic (i.e., entropy of mixing) or physical (i.e., molar

201 volume) aspects of a growing mineral phase (Gresens, 1981; Anderson and Crerar, 1993).  
 202 Thus, for an ideal solid solution the sum of the activity coefficients must equal 1. Under this  
 203 ideal solid solution assumption, the mole fraction,  $x$ , can then be treated as a variable, which  
 204 allows for the traditional net TST (transition state theory) rate laws to be recast such that each  
 205 endmember component can be treated individually as shown below (Eq. 2):

$$206 \quad R_p^{\text{Ge}} = X^{\text{Ge}} k_f A \left( \frac{\text{Ge(OH)}_{4(\text{aq})}}{X^{\text{Ge}} K_{\text{eq}}} - 1 \right)^m \quad (2a)$$

$$207 \quad R_p^{\text{Si}} = X^{\text{Si}} k_f A \left( \frac{\text{Si(OH)}_{4(\text{aq})}}{X^{\text{Si}} K_{\text{eq}}} - 1 \right)^m \quad (2b)$$

$$208 \quad X = \frac{n_{\text{Si,Ge}}}{n_{\text{Si}} + n_{\text{Ge}}} \quad (2c)$$

209 where the individual TST rate laws (in units of mol s<sup>-1</sup>) displayed for Ge ( $R_p^{\text{Ge}}$ , Eq. 2a) and Si  
 210 ( $R_p^{\text{Si}}$ , Eq. 2b) are coupled by the mole fractions for GeO<sub>2(am)</sub> and SiO<sub>2(am)</sub>,  $X$  ( $i = \text{Si, Ge}$ ),  
 211 defined by the number of moles of either Ge or Si ( $n_{\text{Ge,Si}}$ ) over the total moles of amorphous  
 212 silica present (Eq. 2c). These rate equations are dependent on the total surface area of the  
 213 amorphous silica grains ( $A$ , [m<sup>2</sup>]), the rate constants ( $k_f$ , [moles m<sup>-2</sup> s<sup>-1</sup>]), the relative  
 214 activities of the major (Si(OH)<sub>4(aq)</sub>) and trace element (Ge(OH)<sub>4(aq)</sub>) in solution and their  
 215 respective equilibrium constants ( $K_{\text{eq}}$ ). The affinity dependence,  $m$ , is set to 3.5 in this model,  
 216 based on a sensitivity analysis of the reaction order term (which can range from 1 to > 5 for  
 217 amorphous silica precipitation, Iler, 1979; Rimstidt & Barnes, 1980; Fleming, 1986; Tobler et  
 218 al., 2009) performed in Fernandez et al. (2019) for the same experiments. To our knowledge,  
 219 there is no direct constraint for the value of  $m$  across a solid solution between Si and Ge or  
 220 any other comparable system. Thus, the same reaction order term is imposed for both Si and  
 221 Ge rate equations to respect the formalism of the ideal solid solution condition and to  
 222 maintain consistency with the Fernandez et al. (2019) model. Kinetic and equilibrium  
 223 partition coefficients for Ge,  $D_{\text{kin}}$  and  $D_{\text{EQ}}$ , are defined in this model formulation by the ratio

224 of the precipitation rate constants  $\left(\frac{Ge_{Kf}}{Si_{Kf}}\right)$  and equilibrium constants  $\left(\frac{Ge_{Keq}}{Si_{Keq}}\right)$ , respectively, and  
225 are distinct from the overall or ‘effective’ partition coefficient  $K_D \left(\frac{Ge/Si_{solid}}{Ge/Si_{fluid}}\right)$  defined in  
226 **section 1**.

227 This model follows the same fractionation framework initially developed for stable  
228 isotopes (Druhan et al., 2013) and successfully applied to Si stable isotope fractionation for  
229 the same amorphous silica growth experiments (Fernandez et al., 2019). Importantly, the  
230 application of this model to Ge/Si during amorphous silica growth assumes that the behavior  
231 of Ge trace element partitioning is analogous to silicon stable isotopes, as has been indicated  
232 previously for other systems such as  $\delta^{44}\text{Ca}$  and Sr/Ca during calcite growth. Here, for the first  
233 time, we directly test such commonality for the  $\delta^{30}\text{Si}$  and Ge/Si system. This numerical  
234 modeling approach notably allows both fluid and solid phase trace element ratio (Ge/Si)  
235 compositions to evolve through time via coupled net precipitation rates and mole fractions  
236 (Eq. 2) within an ideal solid solution framework. For stable isotopes, the underlying  
237 assumptions for the mole fraction are valid because isotopic substitution into the crystal  
238 structure of a growing solid phase is one of the closest approximations to a true ideality  
239 (Anderson and Crerar, 1993). However, application of the same model to Ge requires  
240 consideration of the appropriateness of this ideal solid solution assumption.

### 241 **2.3.1 The ideal Ge – Si solid solution**

242 The validity of an ideal Ge–Si solid solution for amorphous silica is essentially  
243 unknown due to the lack of available thermodynamic information. Shared chemical properties  
244 (valence state and inorganic aqueous speciation) between Ge and Si implies that Ge  
245 substitution for Si could be reasonably approximated as ideal during secondary silicate  
246 formation (Capobianco and Watson, 1981; Capiobianco and Navrotsky, 1982; Martin et al.,  
247 1996; Pokrovski and Schott, 1998). This recently led Perez-Fodich and Derry (2020) to

248 assume ideality for Ge–Si mixing behavior during kaolinite formation. For the current study  
249 (amorphous SiO<sub>2</sub>–GeO<sub>2</sub> solid solution) two observations are particularly relevant in our  
250 justification of ideality. First, calorimetric data from the Capobianco and Watson (1981)  
251 experimental study of Ge partitioning in sodium feldspars indicate that amorphous glasses  
252 tend to conform better to an ideal solid solution than their crystalline counterparts. Second,  
253 Evans and Derry (2002) found that an ideal solid solution model adequately described the  
254 behavior of Ge and Si during hydrothermal quartz precipitation.

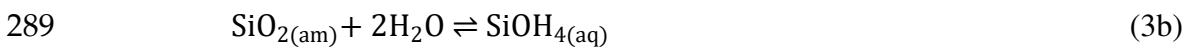
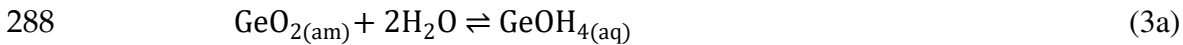
255 Furthermore, Ge/Si in most natural systems is near 10<sup>-6</sup> whereas <sup>30</sup>Si/<sup>28</sup>Si is near  
256 0.031, so while Ge is likely to substitute less readily for <sup>28</sup>Si than <sup>30</sup>Si, its relative abundance  
257 is 4 orders of magnitude lower. With a molar ratio of 10<sup>-5</sup> to 10<sup>-6</sup> between Ge and Si in  
258 silicates, such a system approaches the Henry's Law limit of ideal behavior, even when higher  
259 concentrations would lead to non-ideality. Thus, an ideal solid solution is a reasonable  
260 assumption for Ge–Si binary mixing during amorphous silica growth.

### 261 **2.3.2 Trace element model parameterization**

262 In this model approach, Ge is treated in the same manner as a rare isotopologue in a  
263 stable isotope system, albeit with some important distinctions. For instance, in the treatment  
264 of stable isotopes in this framework, the activities of the individual isotopes (<sup>28</sup>Si and <sup>30</sup>Si)  
265 must sum up to overall activity of Si in solution. But for trace elements, the activities of Ge  
266 and Si are considered independent. Consequently, the kinetic and thermodynamic parameters  
267 of both amorphous SiO<sub>2</sub> and GeO<sub>2</sub> must be acquired individually. Amorphous silica is  
268 fortunately well-studied, and an abundance of kinetic and thermodynamic data are available  
269 from a multitude of carefully conducted laboratory studies (Rimstidt & Barnes, 1980;  
270 Fleming, 1986; Gurnarsson and Arnórsson, 2000, Tobler et al., 2009; Geilert et al., 2014;  
271 Roerdink et al. 2015; Oelze et al. 2015; Stamm et al., 2019; Fernandez et al., 2019). Thus, for  
272 SiO<sub>2</sub>, the precipitation rate and equilibrium constants at 20°C are well constrained with values

273 of  $10^{-9.67}$  moles  $m^{-2} s^{-1}$  (Rimstidt and Barnes, 1980) and  $10^{-2.7135}$  (Gunnarsson and Arnórsson,  
274 2000), respectively. This makes parameterization of Eq. 2a straightforward, as was done in  
275 Fernandez et al. (2019) for the silicon isotope model. Parameterizing Eq. 2b, however, is  
276 more complicated. Experimentally determined thermodynamic data for germanates are scarce  
277 and only exist for a few minerals including argutite ( $GeO_{2(hex)}$ ) (Arnórsson 1984; Pokrovski  
278 and Schott, 1998) and some chain and phyllo-silicates (Pokrovski and Schott, 1998 and  
279 Shtenberg et al., 2017 respectively). We are not currently aware of any kinetic data that exists  
280 for the formation of  $GeO_{2(am)}$ . Lacking this necessary data, we rely on estimates for both  
281 kinetic and thermodynamic parameters based on our experimental results and the known  $K_D$   
282 value of crystalline  $SiO_2$  and  $GeO_2$  phases, respectively.

283 For the amorphous germanium oxide ( $GeO_2$ ) solubility constant, any equilibrium  
284 partitioning between Ge/Si across equilibrated fluid and solid phases implies that this value is  
285 not precisely equal to its  $SiO_2$  counterpart. Assuming applicability to an amorphous solid, we  
286 apply the equilibrium model for an ideal binary mixture between crystalline quartz ( $SiO_2$ ) and  
287 argutite  $GeO_2$ ,  $Ge_xSi_{1-x}O_2$  given by Evans and Derry (2002), which states that:



$$290 \quad GeK_{eq(am)} = \frac{a_{Ge(OH)_4(aq)}}{a_{Si(OH)_4(aq)}} \times \frac{Si_X}{Ge_X} \times SiK_{eq(am)} = \frac{(Ge/Si)_{fluid}}{(Ge/Si)_{solid}} \times SiK_{eq(am)} \quad (3c)$$

$$291 \quad GeK_{eq(am)} \approx \frac{GeK_{sp, argutite}}{SiK_{sp, quartz}} \times SiK_{eq(am)} = D_{EQ(qtz-argutite)} \times SiK_{eq(am)} \quad (3d)$$

292 where for Eq. 3a to Eq. 3c,  $a_{Ge(OH)_4}$  and  $a_{Si(OH)_4}$  are the activities of germanic and silicic acid at  
293 equilibrium,  $Si_X$  and  $Ge_X$  are the mole fractions of the  $SiO_2$  and  $GeO_2$  solid phases, and  
294  $SiK_{eq(am)}$  is the solubility constant for amorphous silica ( $10^{-2.7135}$  M; Gunnarsson and Anórsson,  
295 2000). Through the combination of Eq. 3a and Eq. 3b we can estimate the equilibrium  
296 constant for amorphous  $GeO_2$  (Eq. 3c). The known equilibrium partition coefficient between

297 quartz and argutite ( $D_{EQ} = \frac{{}^{Ge}K_{eq(argutite)}}{{}^{Si}K_{eq(quartz)}}$ ) is defined by their relative equilibrium  
298 constants of  $10^{-3.9582}$  M (Rimstidt and Barnes, 1980) and  $10^{-5.0645}$  M (Pokrovski et al., 2005)  
299 respectively at 25°C. Assuming a comparable partitioning for the amorphous phases and the  
300 known solubility constant for amorphous silica,  ${}^{Si}K_{eq(am)}$ , the equilibrium constant for  
301 amorphous  $GeO_2$  ( ${}^{Ge}K_{eq(am)}$ ) is estimated to be  $10^{-3.8198}$  M (Eq. 3d). Thus,  $D_{EQ}$  for amorphous  
302 silica using the equilibrium model is 0.08, which corresponds to an “effective” partition  
303 coefficient ( $K_D = \frac{(Ge/Si)_{solid}}{(Ge/Si)_{fluid}}$ ) of 12.8 through the expression  $K_D \approx \frac{1}{D_{EQ}}$  (Eq. 3c,d). A  $K_D$  of  
304 12.8 indicates that amorphous silica at equilibrium should have a final Ge/Si ratio 12.8×  
305 higher than the fluid.

306 Ge kinetics during amorphous silica formation are estimated via a best-fit  
307 approximation and sensitivity test using the experimental data reported in this study (**section**  
308 **4.2**). Ge batch model simulations for amorphous silica precipitation were performed for a  
309 range of timescales (35 to 1000 years), surface areas ( $0.072$  to  $50 \text{ m}^2 \text{ g}^{-1}$ ), and Ge precipitation  
310 scenarios using identical starting fluid and solid phase Ge/Si ratios, temperature, and pH.

### 311 **3. RESULTS**

#### 312 **3.1 Time evolution of Ge/Si**

313 Measured fluid and solid phase Ge/Si ratios (denoted as  $(Ge/Si)_{fluid}$  and  $(Ge/Si)_{am.silica}$ ,  
314 respectively; **Table 2**), monitored over the experimental duration from 0 to 30 days (**Fig. 1**),  
315 are presented alongside measured dissolved Si concentrations and their corresponding  $\delta^{30}Si$   
316 values for the high, medium, and low surface area experiments reported by Fernandez et al.  
317 (2019). Dissolved silica concentrations (**Fig. 1A**) decrease with time for all experiments until  
318 a metastable equilibrium is attained with respect to the amorphous silica solubility  
319 concentration at 20°C (Gunnarsson and Anórsson, 2000; Fernandez et al., 2019).  
320 Correspondingly, fluid Ge concentrations ( $Ge(OH)_4$ , **Table 2**) remained relatively constant  
321 with time from a starting concentration of  $44788 \pm 1750 \text{ pM}$  (1SD,  $n = 3$ ) to a final

322 concentration of  $41129 \pm 1989$  pM (1SD,  $n = 3$ ). Of the three batches, the high surface area  
 323 showed the largest variability ( $\text{Ge(OH)}_{4,\text{start}} - \text{Ge(OH)}_{4,\text{end}} = 3921 \pm 1156$  pM). Time averaged  
 324 rates for Ge calculated based on the difference in concentrations over a given time interval  
 325 (Eq. 5 in Fernandez et al. 2019) are  $\sim 5$  orders of magnitude slower ( $R_p^{\text{Ge}} = 10^{-14.3 \pm 0.6}$  mol m<sup>-2</sup>  
 326 s<sup>-1</sup>,  $n = 3$ ; Table 2) than Si precipitation rates ( $R_p^{\text{Si}} = 10^{-8.9 \pm 0.5}$  mol m<sup>-2</sup> s<sup>-1</sup>,  $n = 3$ ; Table 2). For  
 327 all experiments  $(\text{Ge/Si})_{\text{fluid}}$  ratios increase with time and subsequently stabilize at elevated  
 328 values after approximately 10 days (**Fig. 1B**). Low and medium surface area  $(\text{Ge/Si})_{\text{fluid}}$   
 329 values correlate strongly with the corresponding  $\delta^{30}\text{Si}_{\text{fluid}}$ , effectively displaying the same  
 330 evolving behavior with time. In contrast, high surface area  $(\text{Ge/Si})_{\text{fluid}}$  and  $\delta^{30}\text{Si}_{\text{fluid}}$  quickly  
 331 diverge as  $\delta^{30}\text{Si}_{\text{fluid}}$  begins to isotopically re-equilibrate towards lower  $\delta^{30}\text{Si}_{\text{fluid}}$  after roughly 1  
 332 day (Fernandez et al. 2019). Over the same period of time  $(\text{Ge/Si})_{\text{fluid}}$  ratios continue to  
 333 increase and ultimately stabilize to a final  $(\text{Ge/Si})_{\text{fluid}}$  of  $\sim 18.95$   $\mu\text{mol mol}^{-1}$ , which is higher  
 334 than the medium (max  $(\text{Ge/Si})_{\text{fluid}} = 14.40$   $\mu\text{mol mol}^{-1}$ ) and low (max  $(\text{Ge/Si})_{\text{fluid}} = 12.04$   $\mu\text{mol}$   
 335  $\text{mol}^{-1}$ ) surface area batches, respectively.

336 Evolution of the bulk amorphous silica Ge/Si ratios ( $(\text{Ge/Si})_{\text{am.silica}}$ , **Fig. 1B**) were  
 337 calculated based on the cumulative mass of  $\text{SiO}_2$  ( $N_{\text{SiO}_2(\text{ppt})}$  where ppt = precipitate; Fernandez  
 338 et al., 2019) and  $\text{GeO}_2$  ( $N_{\text{GeO}_2(\text{ppt})}$ , **Table 2**) precipitated out of solution onto the pre-existing  
 339 seeds in the batch reactor. Mass balance calculations show  $(\text{Ge/Si})_{\text{am.silica}}$  to slightly increase  
 340 throughout the extent of the reaction compared to the measured initial seed Ge/Si ratios  
 341 (**Table 2**). The high surface area batch shows the largest shifts in the growing amorphous  
 342 silica Ge/Si, from initial value of  $0.28 \pm 0.01$   $\mu\text{mol mol}^{-1}$  to a measured final value of  $0.33$   
 343  $\pm 0.02$   $\mu\text{mol mol}^{-1}$ , which is slightly greater than the analytical uncertainty. This shift to higher  
 344  $(\text{Ge/Si})_{\text{am.silica}}$  values was found to occur after  $\sim 1$  day, by which time a majority of silica has  
 345 been precipitated out of solution ( $\sim 45\%$ ). In comparison, the evolution of  $(\text{Ge/Si})_{\text{am.silica}}$  for  
 346 the lower surface area batches falls within the uncertainty of the measurements ( $\pm 0.02$   $\mu\text{mol}$

347 mol<sup>-1</sup>). The overall increase in the bulk composition observed in the high surface area  
348 experiment, while statistically significant, is small compared with the measured changes in  
349 (Ge/Si)<sub>fluid</sub> as a function of time (**Fig. 1B**).

### 350 **3.2 $\delta^{30}\text{Si}$ vs. Ge/Si**

351 The co-evolution of fluid  $\delta^{30}\text{Si}$  and Ge/Si for all amorphous silica precipitation  
352 experiments are plotted in **Fig. 2**. Starting at initial  $\delta^{30}\text{Si}$  and Ge/Si values of approximately –  
353 2‰ and 8.45  $\mu\text{mol mol}^{-1}$  respectively,  $\delta^{30}\text{Si}_{\text{fluid}}$  and (Ge/Si)<sub>fluid</sub> both increase as a function of  
354 reaction progress through the early stages of the experiments. For the medium and low  
355 surface area batches,  $\delta^{30}\text{Si}_{\text{fluid}}$  and (Ge/Si)<sub>fluid</sub> are linearly correlated (**R<sup>2</sup> = 0.86** and **R<sup>2</sup> = 0.84**,  
356 respectively). However, as observed in the timeseries plot (**Fig. 1B**), a reversal is noted in the  
357 high surface area batch after ~1 day where fluid  $\delta^{30}\text{Si}$  starts to decrease with time while  
358 (Ge/Si)<sub>fluid</sub> ratios continue to increase. This results in a substantial de-correlation between the  
359 high surface area  $\delta^{30}\text{Si}_{\text{fluid}}$  and (Ge/Si)<sub>fluid</sub> at later stages of the reaction.

## 360 **4. DISCUSSION**

### 361 **4.1 Origin of high starting (Ge/Si)<sub>fluid</sub> and potential implications of an evolving reactive** 362 **surface area during dissolution**

363 Relatively constant Ge(OH)<sub>4</sub> concentrations throughout the experimental duration  
364 coupled with rapid Si precipitation and elevated (Ge/Si)<sub>fluid</sub> values suggest that Ge exhibits  
365 slow kinetics during amorphous silica precipitation. However, before proceeding further in  
366 this interpretation, there are two alternative options that could explain the observed data. First,  
367 we consider whether changes in the seed crystal surface area during the partial dissolution of  
368 high surface area seeds at 90°C to prepare our starting solutions could have impacted the rate  
369 of precipitation. In prior amorphous silica studies that served as the basis for our experimental  
370 design (Geilert et al., 2014; Roerdink et al., 2015), this effect is minimized by using a large  
371 quantity of amorphous silica seeds for dissolution at 90°C (10 g L<sup>-1</sup>). Results from mass

372 balance calculations indicate that only 1.65% of the total amount of amorphous silica seed  
373 initially present was dissolved in order to reach Si solubility concentrations at 90°C (5.48  
374 mM; Gunnarsson and Anórrsson, 2000). A simplified geometric model relating mineral  
375 concentration to changes in the reactive surface area (Lichtner, 1988; Noiriél et al. 2009)  
376 suggests that this minor reduction in the solid phase should not impact the corresponding  
377 surface areas of the seeds:

$$378 \quad S = S_0 \left( \frac{C}{C_0} \right)^{-2/3} \quad (4)$$

379 This formulation is based on a shrinking sphere model where S is the final surface area after  
380 dissolution ( $\text{m}^2 \text{g}^{-1}$ ),  $S_0$  is the starting surface area ( $50 \text{ m}^2 \text{g}^{-1}$ ), and  $C_0$  and C corresponds to the  
381 amount of silica in the amorphous phase present prior to and after dissolution ( $\mu\text{moles}$ ). The  
382 calculation indicates an insignificant change in surface area ( $\approx 0.002\%$ ). Furthermore, this  
383 calculation reminds us that dissolution would increase the specific surface area of the  
384 remaining seeds, thus speeding up the reaction and presumably allowing more Ge  
385 incorporation into the growing solid. Although a simplified approach, Eq. 4 supports the  
386 assumptions of Roerdink et al. (2015) and Fernandez et al. (2019) and we proceed with the  
387 understanding that that changes to the surface area are not sufficient to affect our precipitation  
388 rates or the estimation of  $G^{\text{ce}}k_f$  (eq. 2, **section 2.3**).

389 Second, we consider the potential for heterogeneity in the Ge content of the initial  
390 amorphous silica seeds. If the initially elevated  $(\text{Ge}/\text{Si})_{\text{fluid}}$  values were caused by dissolution  
391 of a Ge-enriched rim coating our seed crystals, then rapid re-equilibration with this Ge-  
392 enriched surface layer could sustain high  $(\text{Ge}/\text{Si})_{\text{fluid}}$  values throughout the duration of the  
393 experiment. However, several lines of evidence rebut this option as a likely explanation. To  
394 start, the likelihood of amorphous silica seeds becoming strongly zoned during the fabrication  
395 process is quite low. Assuming a zoned version of our high surface area seeds where the  
396 outermost surface has a Ge/Si ratio of  $\sim 8.45 \mu\text{mol mol}^{-1}$ , mass balance calculations suggest

397 that approximately 50% of the total Ge present in the solid would need to be concentrated in  
398 the upper 0.32 nm of an individual grain perpendicular to its surface. This is smaller than the  
399 size of a unit cell in an SiO<sub>2</sub> crystal structure (0.5405nm for  $\alpha$ -quartz; Ackermann and Sorrel,  
400 1974; Wright and Lehmann, 1981). Finally, high (Ge/Si)<sub>fluid</sub> values with respect to the  
401 dissolving mineral assemblage (0.2 –2.5  $\mu\text{mol mol}^{-1}$ ) are systematically observed at elevated  
402 temperatures with values ranging from 2 to 1000  $\mu\text{mol mol}^{-1}$  (Arnórsson, 1984; Pokrovski and  
403 Schott, 1998; Evans and Derry, 2002; Pokrovski et al., 2005; Escoube et al., 2015). Increasing  
404 (Ge/Si)<sub>fluid</sub> with increasing temperature can be attributed to preferential partitioning of Ge  
405 with respect to Si arising from differences in the thermodynamic properties of Ge(OH)<sub>4(aq)</sub>  
406 and Si(OH)<sub>4(aq)</sub> (Pokrovski and Schott, 1998; Pokrovski et al., 2005). This high temperature  
407 effect is not observed at ambient conditions characteristic of natural terrestrial weathering and  
408 marine environments where (Ge/Si)<sub>fluid</sub> reflects the composition of the dissolving silicate  
409 rocks (Kurtz et al., 2002) and diatoms (Froelich et al., 1984, 1992; Mortlock et al., 1991),  
410 respectively. However, our starting (Ge/Si)<sub>fluid</sub> are consistent with a preferential Ge  
411 partitioning during the pre-dissolution step at 90°C.

412         Regardless, even if the seeds were initially zoned, subsequent rapid re-equilibration  
413 with a Ge-enriched outer surface throughout the extent of the reaction is not possible. Mass  
414 balance calculations show that ~70% of the total Si lost from solution takes place over the  
415 first day, resulting in the formation of a strongly depleted Ge mineral surface that would  
416 effectively isolate the zoned interior from the fluid. Thus, the fluid would only be interacting  
417 and re-equilibrating with the recently-formed mineral surface and a strongly heterogeneous  
418 solid interior would have no effect on the overall (Ge/Si)<sub>fluid</sub>.

419         Having ruled out these complicating effects, we conclude that Ge precipitation kinetics  
420 are slow relative to Si. This offers the simplest and most plausible explanation for our  
421 experimental results. However, in natural settings, it is observed that Ge is (eventually)

422 incorporated into secondary silicates. To determine how slow Ge incorporation is during  
423 amorphous silica formation, we now turn to the application of our trace model under the  
424 assumption that our previous stable isotope fractionation framework (Fernandez et al. 2019)  
425 also describes the partitioning of this trace element.

#### 426 **4.2 Trace model: Ge exchange under a stable isotope fractionation framework**

427 Observed fluid Ge/Si behavior during the amorphous silica growth experiments is  
428 interpreted through a series of numerical simulations adapting the CrunchTope silicon isotope  
429 fractionation model reported in our prior study (Fernandez et al. 2019) to a trace element.  
430 Initial conditions for these numerical experiments are summarized in **Table 3**. Silica kinetic  
431 and thermodynamic parameters for all simulations were kept constant with a log kinetic rate  
432 and equilibrium constant of -9.67 (Rimstidt & Barnes, 1980) and -2.7135 (Gunnarsson and  
433 Anórsson, 2000), respectively (**Table 3**). Potential factors that could influence amorphous  
434 silica solubility concentrations and kinetic rates such as temperature and pH were minimized  
435 via the experimental design. Further, the impact of the surface area and its evolution during  
436 mineral growth on amorphous silica solubility was rigorously examined by Fernandez et al.  
437 (2019) using the Freundlich-Ostwald equation (Enüstun and Turkevich, 1960), finding no  
438 significant changes in the solubility across the three surface area conditions.

439 The equilibrium  $K_D$  imposed ( $D_{eq} = 0.08$ , **Table 3**) derives from our estimated value  
440 based on a quartz–argutite ideal solid solution (further details provided in **section 2.3**). The  
441 kinetic rate constant for the incorporation of dissolved Ge in the solid as  $\text{GeO}_{2(\text{am})}$  was  
442 estimated by an optimization approach where the Ge kinetic rate parameter ( $\log k_{f(\text{GeO}_2)}$ ;  
443 **Table 3**) was altered across a suite of numerical simulations (while keeping  $K_{eq(\text{GeO}_2)}$  and all  
444 other parameters fixed) until an optimal value was found which provided the “best fit” to our  
445 fluid Ge concentration data (**Fig. 3**). The range of kinetic Ge rate constants tested spanned  
446 roughly 6 orders of magnitude from a maximum rate of  $10^{-12.6} \text{ mol m}^{-2} \text{ s}^{-1}$  (~3 orders of

447 magnitude slower than Si) to a minimum rate of  $10^{-26.7}$  mol m<sup>-2</sup> s<sup>-1</sup> (~17 orders of magnitude  
448 slower than Si). Our optimized Ge rate constant value was determined to be  $10^{-19.7 \pm 1.1}$  mol m<sup>-2</sup>  
449 s<sup>-1</sup>, approximately 10 orders of magnitude slower than the Si kinetic rate constant ( $10^{-9.67}$  mol  
450 m<sup>-2</sup> s<sup>-1</sup>; Rimstidt and Barnes, 1980). This yields a kinetic fractionation factor,  $D_{\text{kin}} (^{\text{Ge}}k_f/^{\text{Si}}k_f)$ ,  
451 of  $9.33 \times 10^{-11}$ . A Monte-Carlo sensitivity analysis performed over a broad kinetic and  
452 equilibrium  $K_D$  parameter space further supports our combined estimates for  $K_{\text{eq}(\text{GeO}_2)}$  and  
453  $k_{f(\text{GeO}_2)}$  (**Appendix A**).

454 Flexibility in defining the component of the mineral that contributes to the mole  
455 fraction (X) within the Ge trace model (**section 2.3, Eq. 2**) allows us to test several possible  
456 Ge fluid-mineral mass exchange processes that could describe our observed Ge/Si  
457 partitioning. Three Ge fluid–mineral exchange approaches (Druhan et al., 2013) were  
458 explored in the model, designated respectively as (1) “**no-back reaction**”, (2) “**bulk**”, and (3)  
459 “**surface**”. In the “**no back reaction**” scenario, X is set to the aqueous mole fraction, which  
460 decouples Ge and Si from each other (i.e. the precipitation rate is decoupled from the molar  
461 fraction in the solid) and, thus, only a kinetic fractionation is imposed in the model ( $D_{\text{kin}}$ ). In  
462 this context, Ge and Si evolve irreversibly and the observed  $K_D$  reflects their individual  
463 evolutions along their respective, unidirectional reaction pathways. In the “**bulk**” and  
464 “**surface**” exchange scenarios the fluid and solid phases are allowed to equilibrate with one  
465 another by defining X in terms of the solid mole fraction. Thus,  $D_{\text{EQ}}$  is imposed in these  
466 scenarios as opposed to the “**no back reaction**” case. The most straightforward approach is to  
467 allow the fluid to interact with the total solid or “**bulk**” composition through time. However,  
468 this “**bulk**” approach ignores the potentially significant impact of an evolving or zoning  
469 mineral surface on observed fluid variability during “free-drift” mineral growth. Thus, a  
470 “**surface**” approach was developed in an attempt to address this effect by allowing the fluid  
471 to interact with only the portion of the mineral that has been most recently formed (Druhan et

472 al., 2013; Steefel et al., 2014; Fernandez et al., 2019). In this scenario, the depth into the  
473 mineral surface in contact with the fluid (i.e., the fluid–mineral interaction depth) is  
474 approximated through a running average of the composition of the mass recently precipitated  
475 out of the fluid over a user-defined number of timesteps (details regarding this numerical  
476 implementation can be found in Druhan et al., 2013 and Fernandez et al., 2019). This scenario  
477 implies that the fluid–solid interaction depth varies as a function of reaction progress. This  
478 varying fluid–solid interaction depth is an assumed underlying process which Fernandez et al.  
479 (2019) successfully used to create a forward model of contemporaneous mineral surface and  
480 fluid  $\delta^{30}\text{Si}$  evolution through time. Thus, we now extend this approach to the complementary  
481 Ge/Si system.

### 482 **4.3 Ge partitioning over experimental timescales**

483 The Ge trace model (Eq. 2) generally reproduces our measured fluid Ge/Si evolution  
484 through time across the various surface area conditions (**Fig. 4A**). However,  $(\text{Ge/Si})_{\text{fluid}}$   
485 appears to be less sensitive to the different mass exchange scenarios (“**no back reaction**”,  
486 “**bulk**”, and “**surface**”) over the experimental duration compared to the contemporaneous Si  
487 stable isotope ratios (**Fig. 4B**). This is particularly apparent in the low and medium surface  
488 area cases in which net reaction rates are too slow to distinguish between these three Ge mass  
489 exchange scenarios. The faster kinetics and subsequent re-equilibration of the high surface  
490 area case create a greater response in the  $(\text{Ge/Si})_{\text{fluid}}$  over the 1-month experimental timescale.  
491 Thus, Ge is shown to exhibit quasi-conservative behavior during early (kinetically dominated)  
492 stages of amorphous silica growth.

493 The most promising case for extracting information relevant to Ge incorporation and  
494 the fluid–mineral exchange mechanism underlying observed Ge partitioning lies in the high  
495 surface area experiment. In this case, the system evolved at fast enough rates to capture the  
496 beginning of non-conservative behavior as evidenced by overall greater sensitivity to the

497 different fluid–mineral mass exchange scenarios (**Fig. 4A**). Application of a “**no-back**  
498 **reaction**” model to the measured high surface area  $(\text{Ge/Si})_{\text{fluid}}$  over-predicts the extent of  
499 kinetic partitioning (in a manner comparable to that observed for  $\delta^{30}\text{Si}$ , **Fig. 4B**). The  
500 numerical simulation involving fluid equilibration with the “**bulk**” mineral also fails to  
501 capture experimental  $(\text{Ge/Si})_{\text{fluid}}$  behavior. In this situation, fluid interaction with the total  
502 seed composition ( $0.28 \mu\text{mol mol}^{-1}$ ) predicts a faster decrease in  $(\text{Ge/Si})_{\text{fluid}}$  to values lower  
503 than observed in the experiment.

504 For both  $\text{Ge/Si}$  and  $\delta^{30}\text{Si}$ , the “**surface**” exchange scenario involving fluid interaction  
505 with a co-evolving mineral surface offers the most accurate representation of the high surface  
506 area data. The optimal number of timesteps to average over (i.e., the proxy for the fluid–  
507 mineral interaction depth or the portion of the recently-formed mineral surface in contact with  
508 the fluid) was identified through the same sensitivity analysis performed for  $\delta^{30}\text{Si}$  (**Fig. 4C**,  
509 **D**; Fernandez et al., 2019). This sensitivity analysis yielded a surface equilibration time  
510 interval of  $> 14$  days for the high surface area experimental  $\text{Ge/Si}$  data (**Fig. 4C**), distinctly  
511 larger than that determined for  $\delta^{30}\text{Si}$  (1 day, **Fig. 4D**; Fernandez et al., 2019). The total mass  
512 of newly formed precipitate generated on the high surface area seeds was estimated to  
513 correspond to a depth of 0.19 nm (Fernandez et al., 2019). For the  $\delta^{30}\text{Si}$  study, a time interval  
514 of 1 day implies fast kinetics and fluid interaction with only a very thin portion of the mineral  
515 surface ( $\sim 0.09$  nm, Fernandez et al., 2019). Hence, for the same net amorphous silica  
516 formation rates, a longer time interval (or a greater fluid–mineral surface interaction depth)  
517 for  $\text{Ge/Si}$  implies slower overall kinetics and a relatively longer approach to equilibrium.

518 Therefore, differences in observed fluid  $\delta^{30}\text{Si}$  and  $\text{Ge/Si}$  behavior throughout the  
519 extent of the reaction can be interpreted from a “surface” exchange perspective. For  $\delta^{30}\text{Si}$ ,  
520 faster kinetics and a smaller fluid–mineral surface interaction depth ultimately drives high  
521 surface area  $\delta^{30}\text{Si}_{\text{fluid}}$  to values more negative than the bulk mineral phase ( $-1.81 \pm 0.03 \text{‰}$ ),

522 reflective of the fluid interacting with a strongly  $^{30}\text{Si}$ -depleted mineral surface composition.  
523 On the other hand, slower Ge kinetics and a larger fluid–mineral surface interaction depth  
524 results in  $(\text{Ge}/\text{Si})_{\text{fluid}}$  remaining at elevated values throughout the experimental duration.  
525 Quick precipitation of amorphous silica compared to relatively sluggish Ge incorporation  
526 results in the fluid interacting with a highly depleted Ge/Si mineral surface (**Appendix B, Fig.**  
527 **B.1**). Up to 70% of the total Si precipitated out of solution is generated during the first day of  
528 the experiment. Fluid interaction with this initially low mineral surface Ge/Si composition  
529 shifts  $(\text{Ge}/\text{Si})_{\text{fluid}}$  to values lower than would be predicted in a “no-back reaction” mass  
530 exchange scenario. Due to the relatively small amount of mass precipitated compared to the  
531 total mass of amorphous silica present in the system, the mineral surface is highly sensitive to  
532 any minor incorporation of Ge. Thus, the surface composition is predicted in the model to  
533 increase with time to higher Ge/Si ratios ( $(\text{Ge}/\text{Si})_{\text{ppt}} = 2.81\mu\text{mol mol}^{-1}$ ) in agreement with  
534 simple mass balance approximations using the experimental data (**Table 2**). The ability of the  
535 “surface” option to better predict high surface area data supports a mass exchange between  
536 the fluid and mineral surface as the principal driver of observed  $(\text{Ge}/\text{Si})_{\text{fluid}}$ . Further, a major  
537 finding from these numerical simulations is that Ge/Si and  $\delta^{30}\text{Si}$  have different equilibration  
538 timescales and, thus, represent two distinct “clocks”. In this regard, Ge/Si may serve as a  
539 potent (near)equilibrium tracer in a manner similar to the  $^{29}\text{Si}$  equilibrium tracer (Zheng et al.,  
540 2019; Zhu et al., 2020).

541 This result implies quite distinct kinetic behavior between Ge and Si where Ge kinetic  
542 partitioning is notably slower. Therefore, substantial residence times or path lengths would be  
543 necessary to observe Ge incorporation into secondary phases in natural settings. At first  
544 glance this may appear to contradict a recent study by Perez-Fodich and Derry, 2020, who  
545 used a CrunchTope framework to model Ge/Si incorporation into kaolinite based on field  
546 observations. They suggested that overall fast precipitation rates of kaolinite and comparable

547 Ge and Si kinetics were necessary to explain observed ratios in weathering environments.  
548 However, it should be clarified that Perez-Fodich and Derry (2020) did not directly model  
549 kinetic Ge partitioning during the growth of kaolinite. Rather, they simply note that if  
550 kaolinite growth is slow, Ge incorporation is slow and thus the fluid Ge/Si ratio remains  
551 elevated. Our results are the first to directly illustrate Ge incorporation into secondary  
552 minerals during growth, and clearly show that Ge kinetics are slow relative to Si. This present  
553 study utilizes amorphous SiO<sub>2</sub>, but the results open the possibility that slow Ge kinetics may  
554 also exist for aluminosilicate clays. These findings suggest that the transport timescales in  
555 natural systems may require re-evaluation in light of the unique behavior of Ge kinetics  
556 relative to Si during amorphous silica formation using a direct simulation of Ge kinetics in the  
557 modeling framework presented here.

558         Taking these simulations as a guide, we can now address a driving question in this  
559 study: Is a rate-dependent fractionation framework sufficient to capture both Ge/Si and Si  
560 stable isotope behavior simultaneously in the same system? The answer is a conditional “yes”.  
561 The data-model comparison offers substantial evidence to suggest Ge/Si and  $\delta^{30}\text{Si}$  are self-  
562 consistent during amorphous silica formation. However, this is predicated on the idea that Ge  
563 in the fluid phase interacts with a very different component of the newly formed amorphous  
564 silica surface than its fluid  $\delta^{30}\text{Si}$  counterpart. These findings have significant implications for  
565 how the observed  $K_D$  is defined and interpreted when we extend out to longer timescales.

#### 566 **4.4 Forecasting Ge behavior over long timescales**

567         This section uses the Ge trace model to forecast Ge behavior at longer (annual to  
568 millennial) timescales based on our range of precipitation rates and mineral surface areas.  
569 Since no data are available at these timescales for amorphous silica precipitation to validate  
570 the model predictions, these results should be regarded as hypotheses that we present as a  
571 driver for future research in Ge/Si partitioning during secondary silicate formation. The trace

572 model was run out to 1000 years for all three surface areas, capturing timescales that can be  
573 observed in a wide range of natural system. Only the bulk and surface fluid–mineral exchange  
574 scenarios are used for these simulations as the no back-reaction model will never allow  
575 dissolved Ge to re-equilibrate with the solid phase.

576 Overall, we observe a general trend where the observed partition coefficient,  $K_D$   
577  $((\text{Ge/Si})_{\text{solid}}/(\text{Ge/Si})_{\text{fluid}}$  where solid = bulk  $(\text{Ge/Si})_{\text{am.silica}}$  or cumulatively precipitated  
578  $(\text{Ge/Si})_{\text{ppt}}$  amorphous silica) increases over longer timescales as Ge incorporation is allowed  
579 to proceed (**Fig. 5**). This result corresponds with associated decrease in modeled  $(\text{Ge/Si})_{\text{fluid}}$  to  
580 lower values as a function of time ( $\sim 1.2 \pm 0.2 \mu\text{mol mol}^{-1}$  for the high surface area case,  
581 **Appendix C**). The extent of Ge incorporation into the solid is strongly dependent on the rate  
582 at which equilibrium is approached, which is coupled to the surface area. Importantly, overall  
583 amorphous silica precipitation at these timescales is extremely slow and the system is  
584 functioning at (near) equilibrium conditions. Thus, equilibrium exchange is driving observed  
585 Ge/Si behavior. Despite the obvious limitations in our ability to independently validate such  
586 forecasted Ge/Si partitioning over these timescales, our results consistently demonstrate that  
587 Ge does eventually become incorporated into amorphous silica. Therefore, the general  
588 observation of higher Ge/Si ratios in the solid phase during secondary mineral formation is  
589 eventually recovered in our models at longer annual to decadal timescales.

590 On the experimental timescale, fluid phase  $\delta^{30}\text{Si}$  and Ge/Si were found to be positively  
591 correlated, increasing during early stages of amorphous silica growth. This observation goes  
592 against the inverse relationship between the two tracers that has been previously documented  
593 in the literature for secondary clay formation in field settings (Cornelis et al., 2010; Opfergelt  
594 et al., 2010; Delvigne et al., 2016). There are potentially several reasons for this discrepancy.  
595 Secondary clay formation rates are characteristically slow, as for kaolinite, which has a  
596 precipitation rate that is roughly four orders of magnitude slower than amorphous silica ( $10^{-}$

597  $^{13.6} \text{ mol m}^{-2} \text{ s}^{-1}$ ; Yang and Steefel, 2008). At slow enough precipitation rates, it could be  
598 possible that Ge incorporation occurs at comparable timescales to  $\delta^{30}\text{Si}$  fractionation and,  
599 thus, generates the inverse relationship commonly observed. Results from our long-term Ge  
600 trace model predictions suggest an alternative explanation for this discrepancy, which is  
601 linked to the extent of reactivity in the system and large differences in  $\delta^{30}\text{Si}$  and Ge/Si  
602 equilibration timescales. Field observations could potentially be biased towards equilibrated  
603 systems where observed increases in secondary phase Ge/Si ratios, such as those reported  
604 during storm events in the Rio Icacos watershed in Puerto Rico (Kurtz et al., 2011), may  
605 reflect late-stage mineral recrystallization conditions. However, as we will discuss further in  
606 **section 4.7**, an alternative explanation for such field observations could be associated with  
607 faster Ge uptake reactions such as adsorption and coprecipitation onto iron hydroxides  
608 (Pokrovsky et al., 2006).

609 Finally, results from the Ge trace model highlight the importance of Ge equilibrium  
610 partitioning, which ultimately dominates the long-term evolution of fluid Ge/Si signatures.  
611 Substantial evidence from both our experiments and model runs point to the role of the  
612 mineral surface area in dictating the extent of reaction progress and associated Ge/Si  
613 partitioning during amorphous silica precipitation onto pre-existing seeds. In other words,  
614 high surface areas ( $> 1 \text{ m}^2 \text{ g}^{-1}$ ) “accelerate” whereas lower surface areas ( $< 1 \text{ m}^2 \text{ g}^{-1}$ ) act as  
615 “brakes” on the extent of Ge/Si partitioning. Despite the relatively sluggish Ge incorporation  
616 rates observed in the experiments, we predict that fluid Ge/Si ratios will eventually shift to  
617 lower values typically observed in natural waters ( $\sim 0.6 \pm 0.06 \mu\text{mol mol}^{-1}$ ; Mortlock and  
618 Froelich, 1987). The time that it will take to reach naturally observed Ge/Si ratios is only  
619 approximated in our long-timescale simulations, but our results do appear to overlap with the  
620 average fluid residence times of groundwaters ( $< 50$  years old, Gleeson et al., 2015) and deep  
621 marine sediment porewaters (Bard et al., 1989; Tréguer et al., 1995). From these simulations,

622 Ge/Si partitioning timescales are found to be strongly lagged compared to  $\delta^{30}\text{Si}$  fractionation  
 623 in that Ge incorporation occurs at (near)equilibrium conditions. In other words, despite the  
 624 capability of both systems to express unique kinetic and equilibrium effects, the timescales  
 625 over which kinetic signatures are erased after reaching chemical equilibrium are predicted to  
 626 be quite different for Ge/Si and  $\delta^{30}\text{Si}$ .

## 627 **4.5 The instantaneous partition coefficient, $K_D^{\text{inst}}$ and observed rate dependence**

### 628 *4.5.1 Defining the instantaneous partition coefficient*

629 Even under “chemostatic” conditions where mineral growth occurs under fixed saturation  
 630 states and solute compositions, heterogeneity in the growing mineral surface has been  
 631 observed for Sr/Ca during calcite precipitation (Tang et al., 2008). In the calcite literature, the  
 632 effect of this mineral zoning on the instantaneous partition coefficient was accounted for by  
 633 recasting the traditional method of calculating the partition coefficient (Eq. 5a) in terms of a  
 634 Rayleigh distillation type evolution in the bulk as shown below (Eq. 5b):

$$635 \quad K_D^{\text{inst}} = \frac{\left(\frac{\text{Ge}}{\text{Si}}\right)_{\text{am.silica}}}{\left(\frac{\text{Ge}}{\text{Si}}\right)_{\text{aq}}} \quad (5a)$$

$$636 \quad \left(\frac{\text{Ge}}{\text{Si}}\right)_{\text{am.silica}} = \left(\frac{\text{Ge}}{\text{Si}}\right)_{\text{fluid},0} \times \frac{1 - \left(\frac{\text{Si}}{\text{Si}_0}\right)_{\text{fluid}}^{K_D^{\text{inst}}}}{1 - \left(\frac{\text{Si}}{\text{Si}_0}\right)_{\text{fluid}}} \quad (5b)$$

637 Here these two approaches to calculating  $K_D^{\text{inst}}$  are modified from the Tang et al. (2008) study  
 638 to apply to our Ge/Si data for amorphous silica precipitation. In Eq. 5b,  $\left(\frac{\text{Ge}}{\text{Si}}\right)_{\text{fluid},0}$  represents  
 639 the initial fluid Ge/Si ratio, while  $\left(\frac{\text{Si}}{\text{Si}_0}\right)_{\text{fluid}}$  represents the fraction of Si remaining in solution  
 640 (Si = concentration of dissolved Si at time t,  $\text{Si}_{0,\text{aq}}$  = initial  $\text{SiO}_{2(\text{aq})}$  concentration), and  
 641  $\left(\frac{\text{Ge}}{\text{Si}}\right)_{\text{am.silica}}$  represents a running estimate of bulk amorphous silica composition through time  
 642 (Table 2). Eq. 5b can then be rearranged to solve for the  $K_D^{\text{inst}}$  at each sample interval  
 643 (Appendix D). Our experiments incorporate the additional complexity of “free-drifting”

644 conditions, such that the instantaneous partition coefficient ( $K_D^{inst}$ ) for Ge may be strongly  
645 influenced by heterogeneity in the growing mineral surface. To encapsulate all of these  
646 considerations in the calculation of  $K_D^{inst}$ , we adopt two distinct estimates across all three  
647 surface areas.

648 These approaches to calculating  $K_D^{inst}$  yield distinct values for each surface area tested,  
649 implying that the partition coefficient appears to be rate dependent (**Fig. 6**). All calculated  
650 partition coefficients are  $\ll 1$ , reflecting the artificially high starting fluid Ge/Si ratios that are  
651 caused by an initial  $(Ge/Si)_{fluid}$  that is much higher than the initial ratio of the seed crystals.  
652  $K_D^{inst}$  does not seem to be significantly influenced by the co-evolution of the fluid and bulk  
653 solid Ge/Si ratio during amorphous silica growth. In all cases, the differences between the two  
654 calculated partition coefficients increase with decreasing precipitation rates. Similar  
655 observations for a rate dependent  $K_D^{inst}$  have been reported in the carbonate literature for Sr  
656 trace element partitioning during calcium carbonate formation (Lorens, 1981; Tesoriero and  
657 Pankow, 1996; Huang and Fairchild, 2001; Nehrke et al., 2007; Tang et al., 2008, 2012;  
658 Böhm et al., 2012; Gabitov et al., 2014; AlKhatib and Eisenhauer, 2017). Rate dependence in  
659 these studies were interpreted to reflect greater incorporation of the trace element into the  
660 growing solid at faster precipitation rates. However, based on information from Ge trace  
661 model results at both experimental and longer timescales, the observed rate dependence  
662 cannot be interpreted in the same manner.

#### 663 4.5.2 $K_D^{inst}$ rate dependent behavior for equilibrium tracers

664 For the purpose of this discussion and to allow for these results to be extended to other  
665 systems, our low experimental  $K_D^{inst}$  values determined in **section 4.5.1** were renormalized to  
666 reflect a starting  $(Ge/Si)_{fluid}$  equal to the bulk solid phase composition ( $0.28 - 0.64 \mu\text{mol mol}^{-1}$   
667 <sup>1</sup>). For the experimentally determined values,  $K_D^{inst}$  were normalized by applying the  
668 difference between the initial measured fluid and bulk Ge/Si ratios (i.e.  $(Ge/Si)_{fluid,init} -$

669  $(\text{Ge/Si})_{\text{am.silica,init}}$  to the rest of the measured  $(\text{Ge/Si})_{\text{fluid}}$  values as a function of time.  
670 Normalization of numerically estimated  $K_D^{\text{inst}}$  values was invoked in the Ge trace model by  
671 setting  $(\text{Ge/Si})_{\text{fluid}}$  equal to that of the bulk in the initial conditions and then running the model  
672 out to identical short (35 days) and long (1000 year) times under a “surface” mass exchange  
673 scenario. This renormalization approach is justifiable considering that the Ge trace model  
674 successfully captures observed  $(\text{Ge/Si})_{\text{fluid}}$  variability over the experimental duration (**Fig.**  
675 **4A**).

676 Results of normalized  $K_D^{\text{inst}}$  (denoted from here on as  $K_D^*$ ) are shown in **Fig. 7** as a  
677 function of the amorphous silica precipitation rate ( $R_p$ ) using both the bulk (**Fig. 7A**) and  
678 cumulatively precipitated (**Fig. 7B**) solid compositions over longer timescales. Over the  
679 experimental duration, observed  $K_D^*$  is shown to decrease as  $R_p$  decreases for all surface area  
680 conditions (**Fig. 7C**). However, the relationship between  $K_D^*$  and  $R_p$  eventually flips as we  
681 extend farther into (near)equilibrium conditions during late-stage mineral growth, reflecting a  
682 transition from kinetic to equilibrium partitioning regimes. In the kinetic regime, quasi-  
683 conservative Ge behavior coupled to active silica precipitation results in a newly formed solid  
684 Ge/Si that is initially Ge-depleted, resulting in a decrease in  $K_D^*$  as a function of  $R_p$  (**Fig. 7C**).  
685 Although Ge shows similar rate dependence to those seen in other trace elements (notably Sr  
686 during carbonate formation), the factors underlying this observed correlation between  $K_D^*$  and  
687  $R_p$  are quite distinct. For the trace element Sr, observed decreases in  $K_D^{\text{inst}}$  as a function of the  
688 net precipitation rate reflect uptake rates that are fast enough to “keep up” with carbonate  
689 formation (Gabitov and Watson, 2006; Tang et al., 2008; Wasylenki et al., 2005; AlKhatib  
690 and Eisenhauer, 2017). The opposite is true for Ge, where slow uptake compared to relatively  
691 fast silica precipitation drives the overall relationship between observed  $K_D^{\text{inst}}$  and net  
692 precipitation rates. Ultimately, this kinetic regime is temporary (lasting between a few days to  
693 a month) and quickly transitions into the equilibrium regime characterized by extensive Ge

694 incorporation at (near) equilibrium conditions where Si concentrations no longer change with  
695 time (**Fig. 7 A,B**).

696 These coupled experimental observations and long-term model predictions largely  
697 support an observed rate-dependence in the  $K_D^{inst}$  for amorphous silica that is a direct  
698 consequence of large differences between Si vs. Ge equilibration timescales. This is a major  
699 finding of the study in that: (1) it distinguishes Ge partitioning behavior from other trace  
700 elements, notably Sr but also  $Ba^{2+}$  and  $Cd^{2+}$  (Tesoriero and Pankow, 1996; Prieto et al., 1997),  
701 as a function of the timescale of incorporation; (2) it presents for the first time evidence of  
702 rate-dependent behavior in Ge partition coefficients; and (3) it provides a “conservative-like”  
703 behavior alternative for interpreting rate dependence in the observed  $K_D^{inst}$  for other trace  
704 elements with similarly slow incorporation kinetics. Thus, variability in the observed  $K_D^{inst}$   
705 values we see in nature could reflect a balance between a “conservative” kinetic  $K_D$ , and a  
706 “final” equilibrium  $K_D$ .

#### 707 **4.6 Toward a Ge/Si and $\delta^{30}Si$ multi-tracer approach**

708 Evidence from the experimental data and numerical batch model simulations support the  
709 idea of Ge/Si as an equilibrium tracer. Based on this revised viewpoint, we are now poised to  
710 interpret the  $\delta^{30}Si$  vs Ge/Si relationship observed during amorphous silica precipitation (**Fig.**  
711 **2**). High precipitation rates at the beginning of the reaction result in a strong, positive  
712 correlation between  $\delta^{30}Si$  and Ge/Si until maximum isotope kinetic enrichment is obtained.  
713 Afterwards, as precipitation rates begin to slow down considerably, high surface area  $\delta^{30}Si_{fluid}$   
714 and  $(Ge/Si)_{fluid}$  display a negative correlation where increasing contributions from equilibrium  
715 fractionation return  $\delta^{30}Si_{fluid}$  to values equivalent to or even lower than the starting  
716 composition (referred to as isotopic re-equilibration). Based on the bulk compositions of our  
717 experiments, the  $(Ge/Si)_{fluid}$  at equilibrium is predicted to range from  $\sim 0.02$  to  $0.05 \mu mol mol^{-1}$   
718 <sup>1</sup>. The timescales for  $\delta^{30}Si$  and Ge/Si fractionation are thus drastically different from one

719 another.  $\delta^{30}\text{Si}$  both kinetically fractionates and experiences subsequent re-equilibration before  
720 Ge equilibrium partitioning is even initiated. These  $\delta^{30}\text{Si}$  vs Ge/Si relationships capture a  
721 broad range of secondary mineral progression where high  $\delta^{30}\text{Si}$  and Ge/Si ratios reflect early  
722 stages of formation and low  $\delta^{30}\text{Si}$  and Ge/Si ratios reflect extensive equilibration.

723 Extending to timescales common in natural settings, a combination of trace element  
724 model fluid Ge/Si ratios under a “surface” mass exchange scenario (**section 4.2**) and transient  
725 batch model fluid  $\delta^{30}\text{Si}$  (Fernandez et al., 2019) were run out to 20 years for all surface area  
726 cases (**Fig. 8**). This timescale reflects a typical age of older groundwaters in kinetically  
727 limited weathering environments (Rademacher et al., 2001, 2005; Manning et al., 2012). The  
728 Ge/Si and  $\delta^{30}\text{Si}$  models both predict the extent of equilibrium partitioning to be dependent on  
729 the surface area or rate at which the reaction is allowed to proceed. Precipitation results in a  
730 quasi-hysteresis loop that reflects an interplay between rapid  $\delta^{30}\text{Si}$  kinetic fractionation and  
731 subsequent re-equilibration towards equilibrium values ( $\delta^{30}\text{Si}_{\text{fluid}} = -2.73 \pm 0.07\text{‰}$  calculated  
732 from the starting fluid ratio, Fernandez et al., 2019, and equilibrium fractionation factor,  
733 Stamm et al., 2019) and a slower, continued approach towards predicted  $(\text{Ge/Si})_{\text{fluid}}$   
734 equilibrium values ( $\sim 0.02$  to  $0.05 \mu\text{mol mol}^{-1}$ ) over much longer timescales. Precipitation  
735 onto lower surface area amorphous silica seeds significantly slows down growth rates and  
736 prolongs both Ge/Si and  $\delta^{30}\text{Si}$  disequilibrium. Thus, lower surface area seeds are able to retain  
737 kinetic signatures over much longer timescales.

738 Another way to visualize these  $\delta^{30}\text{Si}$  vs Ge/Si relationships is through the respective  
739 observed Si isotope fractionation factor, (here described via the isotope difference  $\Delta_{\text{solid-fluid}}$   
740  $\approx 1000 \times \ln \alpha$ ) vs. the normalized Ge partition coefficient,  $K_{\text{D}}^*$ , which is here presented in terms  
741 of the cumulative precipitate compositions (**Fig. 9**). In  $\Delta_{\text{solid-fluid}}$  vs.  $K_{\text{D}}^*$  space, a fairly robust  
742 negative correlation is observed between the fractionation factor and partition coefficient  
743 throughout the course of the experiment. Early stages of amorphous silica growth are

744 associated with an increase in  $\Delta_{\text{solid-fluid}}$  (due to mixed kinetic and equilibrium fractionation)  
745 and a decrease in  $K_D^{\text{inst}}$  (due to Ge conservative-like behavior). Late stage evolution of high  
746 surface area  $\Delta_{\text{solid-fluid}}$  and  $K_D^{\text{inst}}$  from model predictions nicely illustrate increasing  
747 contributions from Ge/Si equilibrium partitioning (driving the  $K_D^{\text{inst}}$  up to higher values) as Si  
748 stable isotopes approach (near) equilibrium conditions. Based on these findings, fluid Ge/Si  
749 and  $\delta^{30}\text{Si}$  may provide significant insight into the fluid residence times within the weathering  
750 zone.

751 Finally, we suggest that  $\delta^{30}\text{Si}$  vs Ge/Si relationships can give constraints on the  
752 weathering intensity of a system and the extent of secondary silicate formation where less  
753 intense weathering, kinetically limited environments would express high  $\delta^{30}\text{Si}$  and Ge/Si  
754 signatures and vice versa for more intensely weathered, transport-limited systems. This  
755 application has already been demonstrated for a high weathering intensity, tropical catchment  
756 in Costa Rica (Baronas et al., 2020). Therefore, Ge/Si as a (near)equilibrium tracer serves as a  
757 complement to  $\delta^{30}\text{Si}$ , which has been demonstrated in the recent literature to be a tracer of  
758 kinetic processes (Geilert et al., 2014; Roerdink et al., 2015; Oelze et al., 2015). Further, the  
759 unique behavior of Ge vs.  $\delta^{30}\text{Si}$  with respect to mineralogy serves an added advantage in that  
760 the dissolution and precipitation of a given Ge-bearing silicate can be uniquely identified  
761 within a given system. This combination of complementary trace element and stable isotope  
762 systems represents a path forward in the quantitative analysis of weathering environments,  
763 with its potential only now starting to be realized in the literature (Cardinal et al., 2010;  
764 Cornelis et al., 2010; Opfergelt et al., 2010; Delvigne et al., 2016; Baronas et al., 2018).

#### 765 **4.7 Ge/Si field signatures from a mixed kinetic-equilibrium partitioning perspective**

766 Finally, we take the opportunity to consider observations from a variety of field-scale  
767 systems for which the present study may offer new insight. In transport-limited weathering  
768 environments such as large sedimentary basins where groundwater ages can reach millennial

769 timescales (Sturchio et al., 2004), amorphous silica is commonly observed as a cementation or  
770 accretion between grains and serves as an important  $^{30}\text{Si}$  depleted reservoir (Basile-Doelsch et  
771 al., 2005). In this context, timescales may be sufficient to allow slow Ge incorporation to  
772 serve as a Ge terrestrial sink. At shorter timescales in kinetically limited weathering  
773 environments, amorphous silica formation is less common and most likely a less important  
774 control on observed Ge/Si signatures relative to other secondary phases. However, the range  
775 of surface areas encapsulated by this study ( $0.07 - 50.00 \text{ m}^2 \text{ g}^{-1}$ ) overlap with those observed  
776 in both basaltic ( $2 - 24 \text{ m}^2 \text{ g}^{-1}$ ; Navarre-Stichler et al., 2015) and granitic ( $0.1$  to  $1.5 \text{ m}^2 \text{ g}^{-1}$   
777 White et al., 1996) regolith. Thus, our results may be relevant to other secondary silicates and  
778 suggest that if slow Ge kinetics are indeed applicable to a variety of secondary clays, then  
779 long subsurface fluid transit times would be necessary to create low stream Ge/Si  
780 compositions as a result of Ge incorporation into these minerals. If Ge incorporation into  
781 secondary clays is slow because of kinetic limitations on either mineral neof ormation or Ge  
782 incorporation into neoformed phases then adsorption onto Fe and Al (oxy)hydroxides may  
783 play a more important role on shorter timescales (Mortlock and Froelich, 1987; Kurtz et al.,  
784 2002; Schribner et al., 2006). For instance, batch experiments showed fast Ge uptake rates  
785 during for Ge adsorption onto goethite, with  $\sim 80\%$  of dissolved Ge removed from solution  
786 over the span of 10 minutes and complete Ge incorporation by 100 minutes during  
787 coprecipitation with FeOH (Pokrovsky et al., 2006).

788 Slow Ge kinetics and mixed kinetic and equilibrium Ge partitioning may also hold  
789 relevance for the signatures of marine diagenesis. Observations of Ge decoupling from Si at  
790 depth in marine sediments rich in biogenic opal spanning 100,000s of years (Hammond et al.,  
791 2000; King et al., 2000; Baronas et al., 2016) have generally been interpreted as reflecting a  
792 complex balance between biogenic silica dissolution and (re)precipitation of amorphous silica  
793 along with potentially iron-rich clays. From the perspective of our experimental results,

794 decoupling of Ge from Si could reflect the large disparity between fast Si precipitation  
795 kinetics and slow Ge recrystallization, yielding observations of Ge-enriched porewaters with  
796 depth into the sediment profile (King et al., 2000).

797 Finally, results from this study may offer utility in the interpretation of high Ge/Si ratios  
798 found in hydrothermal waters (Arnórsson, 1984; Criaud and Fouillac, 1986; Evans and Derry,  
799 2002; Han et al., 2015). Geothermal waters from active geothermal systems have high, but  
800 variable  $(\text{Ge/Si})_{\text{fluid}}$ , which was explained using a Rayleigh model for the precipitation of Ge-  
801 depleted quartz along a cooling path(s) (Evans and Derry 2002). Our findings agree with this  
802 interpretation where the formation of Ge-depleted amorphous silica would result in elevated  
803  $(\text{Ge/Si})_{\text{fluid}}$  throughout the experimental duration. However, the successful application of our  
804 trace model to the experimental data suggest that a Rayleigh model could be overly simplistic  
805 of an approach for amorphous silica where a back reaction is known to occur and would most  
806 likely lead to an overestimation of the extent of Ge/Si partitioning. Our combined modeling  
807 and experimental study concludes that fluid interaction with the mineral surface dictates the  
808 observed  $(\text{Ge/Si})_{\text{fluid}}$  over the timescales of mineral growth.

## 809 **5. CONCLUSIONS**

810 This study reports Ge/Si fractionation during amorphous silica precipitation across a range  
811 of precipitation rates under highly controlled laboratory settings. Our findings show that Ge  
812 incorporation kinetics are very slow (~ 10 orders of magnitude slower than silica precipitation  
813 rates) and, as a result, gives the appearance of conservative behavior over short timescales (~  
814 30 days). A major consequence of this observed lag between fast Si kinetics and Ge  
815 conservative-like behavior at early stages of mineral growth is the appearance of rate  
816 dependence behavior in the observed partition coefficient,  $K_D$ . Model results imply that Ge/Si  
817 fractionation is controlled strictly by equilibrium processes, making it a unique equilibrium  
818 tracer. Over long timescales, Ge/Si equilibrium partitioning appears to exhibit dependence on

819 the reaction rate with fluid Ge/Si returning to equilibrium values faster during uptake onto  
820 higher surface area seeds relative to lower surface area seeds. A combined  $\delta^{30}\text{Si}$  and Ge/Si  
821 multi-tracer approach has the potential to provide important constraints on weathering  
822 intensity, fluid residence times and the amount of secondary silicate formation taking place in  
823 the weathering zone. Finally, successful application of the trace element batch model to the  
824 experimental dataset over a range of surface areas suggests that the framework developed in  
825 the CrunchTope software under the assumption that trace elements behave analogously to  
826 stable isotopes is valid for germanium. Our results extend the utility of CrunchTope for  
827 modeling both kinetic and equilibrium trace element partitioning in addition to stable isotope  
828 fractionation.

829

### 830 **ACKNOWLEDGMENTS**

831

832 This material is based upon work supported by the National Science Foundation Graduate  
833 Research Fellowship Program under Grant No. DGE-1144245, NSF grant EAR 1660923,  
834 l'Agence Nationale de la Recherche project ANR-17-MPGA-0009, and by the Chateaubriand  
835 Fellowship of the Office for Science & Technology of the Embassy of France in the United  
836 States. Special acknowledgment is given to Jérôme Gaillardet, Julien Bouchez, and the G2E  
837 (Géochimie des Enveloppes Externes) group for their assistance and allowing us access to the  
838 facilities at the Institut de Physique du Globe de Paris (IPGP) in Paris, France to perform the  
839 experiments and measurements necessary for this study.

840

841

842

843

### 844 **REFERENCES**

845

846 Ackermann R. J. and Sorrell C. A.(1974) Thermal expansion and the high-low transformation  
847 in quartz. I. High-temperature X-ray studies. *J. Appl.Crystallogr.* **7**, 461–467.

848 Aguirre A. A., Derry L. A., Mills T. J., Anderson S. P. (2017) Colloidal transport in the  
849 Gordon Gulch catchment of the Boulder Creek CZO and its effect on C-Q relationships for  
850 silicon. *Water Resour. Res.* **53**, 2368–2383.

851 AlKhatib M. and Eisenhauer A. (2017) Calcium and strontium isotope fractionation in  
852 aqueous solutions as a function of temperature and reaction rate: I. Calcite. *Geochim.*  
853 *Cosmochim. Acta* **209**, 296–319.

854 Ameijeiras-Marino Y., Opfergelt S., Derry L. A., Robinet J., Govers G., Minella J. P. G., and  
855 Delmelle P. (2018) Ge/Si ratios point to increased contribution from deeper mineral  
856 weathering to streams after forest conversion to cropland. *Applied Geochemistry* **96**, 24–34.

857 Anderson G. M. and Crerar D. A. (1993) Thermodynamics in Geochemistry: The Equilibrium  
858 Model. Oxford University Press, London.

859 Arnórsson, S. (1984) Germanium in Icelandic geothermal systems. *Geochim. Cosmochim.*  
860 *Acta* **48**, 2489–2502.

861 Bard E., Labeyrie L. D., Arnold M., Labracherie M., Pichon J.-L. Duprat J., and Duplessy J.-  
862 C. (1989) AMS 14-C ages measured in deep-sea cores from the Southern Ocean: implications  
863 for the sedimentation rates during isotope stage 2. *Quaternary Research* **31**, 309–317.

864 Baronas J. J., Hammond D. E., Berelson W. M., McManus J., and Severmann S. (2016)  
865 Germanium-silicon fractionation in a river-influenced continental margin: The Northern Gulf  
866 of Mexico. *Geochim. Cosmochim. Acta* **178**, 124–142.

867 Baronas J. J., Torres M. A., West A. J., Rouxel O., George B., Bouchez J., Gaillardet J. and  
868 Hammond D. E. (2018) Ge and Si isotope signatures in rivers: A quantitative multi-proxy  
869 approach. *Earth Planet. Sci. Lett.* **503**, 194–215.

870 Baronas J. J., West A. J., Burton K. W., Hammond D. E., Opfergelt S., Pogge von  
871 Strandmann P. A. E., James R. H., and Rouxel O. J. (2020) Ge and Si isotope behavior during  
872 intense tropical weathering and ecosystem cycling. *Global Biogeochemical Cycles* **34**, 1–25.

873 Basile-Doelsch I., Meunier J. D., and Parron C. (2005) Another continental pool in the  
874 terrestrial silicon cycle. *Nature* **433**, 399–402.

875 Blecker S. W., King S. L., Derry L. A., Chadwick O. A., Ippolito J. A., Kelly E. F. (2007)  
876 The ratio of germanium to silicon in plant phytoliths: quantification of biological  
877 discrimination under controlled experimental conditions. *Biogeochemistry* **86**, 189–199.

878 Böhm F., Eisenhauer A., Tang J., Dietzel M., Krabbenhöft A., Kiskirek B., Horn C. (2012)  
879 Strontium isotope fractionation of planktic foraminifera and inorganic calcite. *Geochim.*  
880 *Cosmochim. Acta* **93**, 300–314.

881 Capobianco C. and Navrotsky A. (1982) Calorimetric evidence for ideal mixing of silicon and  
882 germanium in glasses and crystals of sodium-feldspar composition. *Am. Mineral.* **67**, 718–  
883 724.

884 Capobianco C. and Watson E. B. (1981) Olivine/silicate melt partitioning of germanium: an  
885 example of a nearly constant partition coefficient. *Geochim. Cosmochim. Acta* **46**, 235–240.

886 Cardinal D., Gaillardet J., Hughes H. J., Opfergelt S. and André L. (2010) Contrasting silicon  
887 isotope signatures in rivers from the Congo Basin and the specific behaviour of organic-rich  
888 waters. *Geophys. Res. Lett.* **37**.

889 Cornelis J. T., Delvaux B. and Titeux H. (2010) Contrasting silicon uptakes by coniferous  
890 trees: A hydroponic experiment on young seedlings. *Plant Soil* **336**, 99–106.

891 Criaud A. and Fouillac C. (1986) Study of CO<sub>2</sub>-rich thermomineral waters from the central  
892 French massif. 2. Behavior of some trace-metals, arsenic, antimony and germanium.  
893 *Geochim. Cosmochim. Acta* **50**, 1573–1582.

894 Delvigne C., Opfergelt S., Cardinal D., Delvaux B., and André L. (2009) Distinct silicon and  
895 germanium pathways in the soil–plant system: Evidence from banana and horsetail. *J.*  
896 *Geophys. Res.* **114**, 1–11.

897 Delvigne C., Opfergelt S., Cardinal D., Hofmann A. and André L. (2016) Desilication in  
898 Archean weathering processes traced by silicon isotopes and Ge/Si ratios. *Chem. Geol.* **420**,  
899 139–147.

900 DePaolo D. J. (2011) Surface kinetic model for isotopic and trace element fractionation  
901 during precipitation of calcite from aqueous solutions. *Geochim. Cosmochim. Acta* **75**, 1039–  
902 1056.

903 Derry L. A., Kurtz A. C., Ziegler K. and Chadwick O. A. (2005) Biological control of  
904 terrestrial silica cycling and export fluxes to watersheds. *Nature* **433**, 728–731.

905 Druhan J. L., Steefel C. I., Williams K. H. and DePaolo D. J. (2013) Calcium isotope  
906 fractionation in groundwater: Molecular scale processes influencing field scale behavior.  
907 *Geochim. Cosmochim. Acta* **119**, 93–116.

908 Escoube R., Rouxel O. J., Edwards K., Glazer B., and Donard O. F. X. (2015) Coupled Ge/Si  
909 and Ge isotope ratios as geochemical tracers of seafloor hydrothermal systems: Case studies  
910 at Loihi Seamount and East Pacific Rise 9°50'N. *Geochim. Cosmochim. Acta* **167**, 93–112.

911 Evans M. J. and Derry L. A. (2002) Quartz control of high germanium/silicon ratios in  
912 geothermal waters. *Geology* **30**, 1019–1022.

913 Fernandez N. M., Zhang X. and Druhan J. L. (2019) Silicon isotopic re-equilibration during  
914 amorphous silica precipitation and implications for isotopic signatures in geochemical  
915 proxies. *Geochim. Cosmochim. Acta* **262**, 104–127.

916 Fleming B. A. (1986) Kinetics of reaction between silicic acid and amorphous silica surfaces  
917 in NaCl solutions. *J. Colloid Interface Sci.* **110**, 40–64.

918 Frings P. J., Clymans W., Fontorbe G., De La Rocha C. L. and Conley D. J. (2016) The  
919 continental Si cycle and its impact on the ocean Si isotope budget. *Chem. Geol.* **425**, 12–36.

920 Froelich P. N., Blanc V., Mortlock R. A., Chillrud S. N., Dunstan W., Udomkit A. and Peng  
921 T.-H. (1992) River fluxes of dissolved silica to the ocean were higher during glacials: Ge/Si  
922 in diatoms, rivers, and oceans. *Paleoceanography* **7**, 739–767.

923 Froelich P. N., Hambrick G.A. Andreae M. O., Mortlock R. A. and Edmond J. M. (1985) The  
924 geochemistry of inorganic germanium in natural waters. *J. Geophys. Res. Ocean.* **90**, 1133–  
925 1141.

926 Froelich P. N., Hambrick G. A., Kaul L. W., Byrd J. T., and Lecoite O. (1984) Geochemical  
927 behavior of inorganic germanium in an unperturbed estuary. *Geochim. Cosmochim. Acta* **49**,  
928 519–524.

929 Gabitov R. I. and Watson E. B. (2006) Partitioning of strontium between calcite and fluid.  
930 *Geochemistry, Geophys. Geosystems* **7**, 1–12.

931 Gabitov R. I., Sadekov A. and Leinweber A. (2014) Crystal growth rate effect on Mg/Ca and  
932 Sr/Ca partitioning between calcite and fluid: An in situ approach. *Chem. Geol.* **367**, 70–82.

933 Geilert S., Vroon P. Z., Roerdink D. L., Van Cappellen P. and van Bergen M. J. (2014)  
934 Silicon isotope fractionation during abiotic silica precipitation at low temperatures: Inferences  
935 from flow-through experiments. *Geochim. Cosmochim. Acta* **142**, 95–114.

936 George R. B., Reynolds B. C., Frank M. and Halliday A. N. (2006) Mechanisms controlling  
937 the silicon isotopic compositions of river waters. *Earth Planet. Sci. Lett.* **249**, 290–306.

938 George R. B., Reynolds B. C., West A. J., Burton K. W. and Halliday A. N. (2007) Silicon  
939 isotope variations accompanying basalt weathering in Iceland. *Earth Planet. Sci. Lett.* **261**,  
940 476–490.

941 George R. B., Zhu C., Reynolds B.C. and Halliday A.N. (2009) Stable silicon isotopes of  
942 groundwater, feldspars, and clay coatings in the Navajo Sandstone aquifer, Black Mesa,  
943 Arizona, USA. *Geochim. Cosmochim. Acta* **73**, 2229–2241.

944 Gleeson T., Befus K. M., Jasechko S., Luijendijk E., Bayani Cardenas M. (2015) The global  
945 volume and distribution of modern groundwater. *Nature* **9**, 161–167.

946 Goldschmidt V. M. (1926) Concerning the crystallo-chemical and geochemical behavior of  
947 Germanium. *Naturwissenschaften* **14**, 295–297.

948 Goldschmidt V.M. (1958) *Geochemistry*. Oxford University Press, London.

949 Gresens R. L. (1981) The aqueous solubility product of solid solutions: 1. Stoichiometric  
950 saturation: partial and total solubility product. *Chem. Geol.* **32**, 59–72.

951 Gunnarsson I. and Anórsson S. (2000) Amorphous silica solubility and the thermodynamic  
952 properties of  $H_4SiO_4$  in the range of 0° to 350°C at Psat. *Geochim. Cosmochim. Acta* **64**,  
953 2295–2307.

954 Hammond D. E., McManus J., Berelson W. M., Meredith C., Klinkhammer G. P., and Coale  
955 K. H. (2000) Diagenetic fractionation of Ge and Si in reducing sediments: The missing Ge  
956 sink and a possible mechanism to cause glacial/interglacial variations in oceanic Ge/Si.  
957 *Geochim. Cosmochim. Acta* **64**, 2453–2465.

958 Han Y., Huh Y., and Derry L. (2015) Ge/Si ratios indicating hydrothermal and sulfide  
959 weathering input to rivers of the Eastern Tibetan Plateau and Mt. Baekdu. *Chem. Geol.* **410**,  
960 40–52.

961 Heumann K.G. (1988) Isotope Dilution Mass Spectrometry, in: Adams F., Gijbels R., van  
962 Grieken R., (Eds.), *Inorganic Mass Spectrometry*. John Wiley & Sons, New York, NY.

963 Huang Y. and Fairchild I. J. (2001) Partitioning of  $Sr^{2+}$  and  $Mg^{2+}$  into calcite under karst-  
964 analogue experimental conditions. *Geochim. Cosmochim. Acta* **65**, 47–62.

965 Hughes H. J., Sondag F., Santos R. V., André L. and Cardinal D. (2013) The riverine silicon  
966 isotope composition of the Amazon Basin. *Geochim. Cosmochim. Acta* **121**, 637–651.

967 Iler R. K. (1979) *The Chemistry of Silica: Solubility, Polymerization, Colloid and Surface*  
968 *Chemistry, and Biochemistry*., John Wiley & Sons.

969 King S. L., Froelich P. N., and Jahnke R. A. (2000) Early diagenesis of germanium in  
970 sediments of the Antarctic South Atlantic: In search of the missing Ge sink. *Geochim.*  
971 *Cosmochim. Acta* **64**, 1375–1390.

972 Kurtz A. C., Derry L. A. and Chadwick O. A. (2002) Germanium-silicon fractionation in the  
973 weathering environment. *Geochim. Cosmochim. Acta* **66**, 1525–1537.

974 Kurtz A.C., Lugolobi F. and Salvucci G. (2011) Germanium–silicon as a flow path tracer:  
975 Application to the Rio Icacos watershed. *Water Resour. Res.* **47**, 1–16.

976 Lichtner P. C. (1988) The quasi-stationary state approximation to coupled mass transport and  
977 fluid-rock interaction in a porous medium. *Geochim. Cosmochim. Acta* **52**, 143–165.

978 Lorens R. B. (1981) Sr, Cd, Mn and Co distribution coefficients in calcite as a function of  
979 calcite precipitation rate. *Geochim. Cosmochim. Acta* **45**, 553–561.

980 Lugolobi F., Kurtz A. C. and Derry L. A. (2010) Germanium–silicon fractionation in a  
981 tropical, granitic weathering environment. *Geochim. Cosmochim. Acta* **74**, 1294–1308.

982 Manning A. H., Clark J. F., Diaz S. H., Rademacher L. K., Earman S., and Plummer L. N.  
983 (2012) Evolution of groundwater age in a mountain watershed over a period of thirteen years.  
984 *J.Hydrol.***460-461**, 13–28.

985 Martin F., Ildefonse P., Hazemann J. L., Petit S., Grauby O., Decarreau A. (1996) Random  
986 distribution of Ge and Si in synthetic talc: An EXAFS and FTIR study. *Eur. J. Mineral.* **8**,  
987 289–299.

988 Meek K., Derry L., Sparks J., Cathles L. (2016) 87/86Sr, Ca/Sr, and Ge/Si ratios as tracers of  
989 solute sources and biogeochemical cycling at a temperate forested shale catchment, central  
990 Pennsylvania, USA. *Chem. Geol.* **445**, 84–102.

991 Mortlock R.A. and Froelich P.N. (1987) Continental weathering of germanium: Ge/Si in the  
992 global river discharge. *Geochim. Cosmochim. Acta* **51**, 2075–2082.

993 Mortlock R.A. and Froelich P.N. (1996) Determination of germanium by isotope dilution  
994 hydride generation inductively coupled plasma mass spectrometry. *Analytica Chimica Acta*  
995 **332**, 277-284.

996 Mortlock R.A., Charles C.D., Froelich P.N., Zibello M.A., Saltzman J., Hays J.D., and  
997 Burckle L.H. (1991) Evidence for lower productivity in the Antarctic Ocean during the last  
998 glaciation. *Nature* **351**, 220–222.

999 Murnane R. J. and Stallard R.F. (1990) Germanium and silicon in rivers of the Orinoco  
1000 drainage basin. *Nature* **344**, 749.

1001 Navarre-Stichler A., Brantley S.L., and Rother G. (2015) How porosity increases during  
1002 incipient weathering of crystalline silicate rocks. *Reviews Mineral. Geochem.* **80**, 331–354.

1003 Nehrke G., Reichart G.J., Van Cappellen P., Meile C., Bijma J. (2007) Dependence of calcite  
1004 growth rate and Sr partitioning on solution stoichiometry: Non-Kossel crystal growth.  
1005 *Geochim. Cosmochim. Acta* **71**, 2240–2249.

1006 Noiriél C., Luquot L., Madé B., Raimbault L., Gouze P., and van der Lee J. (2009) Changes  
1007 in reactive surface area during limestone dissolution: An experimental and modeling study.  
1008 *Chem. Geol.* **265**, 160–170.

1009 Oelze M., von Blanckenburg F., Bouchez J., Hoellen D. and Dietzel M. (2015) The effect of  
1010 Al on Si isotope fractionation investigated by silica precipitation experiments. *Chem. Geol.*  
1011 **397**, 94–105.

1012 Opfergelt S., Cardinal D., André L., Delvigne C., Bremond L. and Delvaux B. (2010)  
1013 Variations of  $\delta^{30}\text{Si}$  and Ge/Si with weathering and biogenic input in tropical basaltic ash soils  
1014 under monoculture. *Geochim. Cosmochim. Acta* **74**, 225–240.

1015 Opfergelt S. and Delmelle P. (2012) Silicon isotopes and continental weathering processes:  
1016 Assessing controls on Si transfer to the ocean. *Comptes Rendus Geosci.* **344**, 723–738.

1017 Perez-Fodich, A. and Derry, L.A. (2020) A model for germanium-silicon equilibrium  
1018 fractionation in kaolinite. *Geochimica Et Cosmochimica Acta* 288, 199-213.

1019 Pogge von Strandmann P. A. E., Opfergelt S., Lai Y.-J., Sigfússon B., Gislason S. R. and  
1020 Burton K. W. (2012) Lithium, magnesium and silicon isotope behaviour accompanying  
1021 weathering in a basaltic soil and pore water profile in Iceland. *Earth Planet. Sci. Lett.* **339–**  
1022 **340**, 11–23.

1023 Pokrovski G. S. and Schott J. (1998) Experimental study of the complexation of silicon and  
1024 germanium with aqueous organic species: implications for germanium and silicon transport  
1025 and Ge/Si ratio in natural waters. *Geochim. Cosmochim. Acta* **62**, 3413–3428.

1026 Pokrovski G.S., Roux J., Hazemann J–L., Testemale D. (2005) An X-ray absorption  
1027 spectroscopy study of argutite solubility and aqueous Ge(IV) speciation in hydrothermal  
1028 fluids to 500 °C and 400 bar. *Chem. Geo.* **217**, 127–145.

1029 Pokrovsky O.S., Pokrovski G.S., Schott J., and Galy A. (2006) Experimental study of  
1030 germanium adsorption on goethite and germanium coprecipitation with iron hydroxide: X-ray  
1031 absorption fine structure and macroscopic characterization. *Geochim. Cosmochim. Acta* **70**,  
1032 3325–3341.

1033 Prieto M., Fernández-González A., Putnis A., and Fernández-Díaz L. (1997) Nucleation,  
1034 growth, and zoning phenomena in crystallizing (Ba,Sr)CO<sub>3</sub>, Ba(SO<sub>4</sub>, CrO<sub>4</sub>), (Ba,Sr)SO<sub>4</sub>, and  
1035 (Cd,Ca)CO<sub>3</sub> solid solutions from aqueous solutions. *Geochim. Cosmochim. Acta* **61**, 3383–  
1036 3397.

1037 Qi H.W., Hu R.Z., Jiang K., Zhou T., Liu Y.F., and Xiong Y.W. (2019) Germanium isotopes  
1038 and Ge/Si fractionation under extreme tropical weathering of basalts from the Hainan Island,  
1039 South China. *Geochim. Cosmochim. Acta* **253**, 249–266.

1040 Rademacher L.K., Clark J.F., Clow D.W., and Hudson G.B. (2005) Old groundwater  
1041 influence on stream hydrochemistry and catchment response times in a small Sierra Nevada  
1042 catchment: Sagehen Creek, California. *Water. Resour. Res.* **41**, 1–10.

1043 Rademacher L.K., Clark J.F., Hudson G.B., Erman D.C., Erman N.A. (2001) Chemical  
1044 evolution of shallow groundwater as recorded by springs, Sagehen basin, Nevada County,  
1045 California. *Chem. Geol.* **179**, 37–51.

1046 Rimstidt J. D. and Barnes H. L. (1980) The kinetics of silica-water reactions. *Geochim.*  
1047 *Cosmochim. Acta* **44**, 1683–1699.

1048 Riotte J., Meunier J. -D., Zambardi T., Audry S., Barboni D., Anupama K., Prasad S.,  
1049 Chmeleff J., Poitrasson F., Sekhar M. and Braun J.-J. (2018) Processes controlling silicon  
1050 isotopic fractionation in a forested tropical watershed: Mule Hole Critical Zone Observatory  
1051 (Southern India). *Geochim. Cosmochim. Acta* **228**, 301–319.

1052 Roerdink D. L., van den Boorn S. H. J. M., Geilert S., Vroon P. Z. and van Bergen M. J.  
1053 (2015) Experimental constraints on kinetic and equilibrium silicon isotope fractionation  
1054 during the formation of non-biogenic chert deposits. *Chem. Geol.* **402**, 40–51.

1055 Scribner A. M., Kurtz A. C. and Chadwick O. A. (2006) Germanium sequestration by soil:  
1056 Targeting the roles of secondary clays and Fe-oxyhydroxides. *Earth Planet. Sci. Lett.* **243**,  
1057 760–770.

1058 Shtenberg M.V., Bychinskii V.A., Koroleva O.N., Korobatova N.M., Tupitsyn A.A.,  
1059 Fomichev S.V., and Krenev V.A. (2017) Calculation of the formation enthalpies, standard  
1060 entropies, and standard heat capacities of alkali and alkaline-earth germanates. *Russian*  
1061 *Journal of Inorganic Chemistry* **62**, 1464–1468.

1062 Stamm F.M., Zambardi T., Chmeleff J., Schott J., von Blanckenburg F., Oelkers E.H. (2019)  
1063 The experimental determination of equilibrium Si isotope fractionation factors among

1064  $\text{H}_4\text{SiO}_4^0$ ,  $\text{H}_3\text{SiO}_4^-$  and amorphous silica ( $\text{SiO}_2 \cdot 0.32 \text{H}_2\text{O}$ ) at 25 and 75°C using the three-  
1065 isotope method. *Geochim. Cosmochim. Acta* **255**, 49–68.

1066 Steefel C.I., Druhan J.L., and Maher K. (2014) Modeling coupled chemical and isotopic  
1067 equilibration rates. *Procedia Earth Planet.* **10**, 208–217.

1068 Steefel C. I., Yabusaki S. B. and Mayer K. U. (2015) Reactive transport benchmarks for  
1069 subsurface environmental simulation. *Comput. Geosci.* **19**, 439–443.

1070 Sturchio N.C., Du X., Purtschert R., Lehmann B.E., Sultan M., Patterson L.J. Müller P.,  
1071 Bigler T., Bailey K., O'Connor T.P., Young L., Lorenzo R., Becker R., El Alfy Z., Kaliouby  
1072 B.El. Dawood Y., and Abdallah A.M.A. One million year old groundwater in the Sahara  
1073 revealed by krypton-81 and chlorine-36. *Geophys. Res. Lett.* **31**, 1–4.

1074 Tang J., Köhler S. J. and Dietzel M. (2008)  $\text{Sr}^{2+}/\text{Ca}^{2+}$  and  $^{44}\text{Ca}/^{40}\text{Ca}$  fractionation during  
1075 inorganic calcite formation: I. Sr Incorporation. *Geochim. Cosmochim. Acta* **72**, 3718–3732.

1076 Tesoriero, A.J. and Pankow, J.F. (1996) Solid solution partitioning of  $\text{Sr}^{2+}$ ,  $\text{Ba}^{2+}$ , and  $\text{Cd}^{2+}$  to  
1077 calcite. *Geochim. Cosmochim. Acta* **60**, 1053–1063.

1078 Tobler D. J., Shaw S. and Benning L. G. (2009) Quantification of initial steps of nucleation  
1079 and growth of silica nanoparticles: An in-situ SAXS and DLS study. *Geochim. Cosmochim.*  
1080 *Acta* **73**, 5377–5393.

1081 Tréguer P., Nelson D.M., van Bennekom A.J., DeMaster D.J., Leynaert A., Quéguiner B.  
1082 (1995) The balance of silica in the world oceans: a re-estimate. *Science* **268**, 375–379.

1083 Wada S. and Wada K. (1982) Effects of substitution of germanium for silicon in imogolite.  
1084 *Clays and Clay Minerals* **30**, 123–128.

1085 Wasylenki L.E., Dove P.M., Wilson D.S., and De Yoreo J.J. (2005) Nanoscale effects of  
1086 strontium on calcite growth: An in-situ AFM study in the absence of vital effects. *Geochim.*  
1087 *Comochim. Acta* **69**, 3017–3027.

1088 White A.F., Blum A.E., Schulz M.S., Bullen T.D., Harden J.W., and Peterson M.L.(1996)  
1089 Chemical weathering rates of a soil chronosequence on granitic alluvium: I. Quantification of  
1090 mineralogical and surface area changes and calculation of primary silicate reaction rates.  
1091 *Geochim. Cosmochim. Acta* **60**, 2533–2550.

1092 Wright A.F. and Lehmann M.S.(1981) The structure of quartz at 25 and 590°C determined by  
1093 neutron diffraction. *J. Solid State Chem.* **36**, 371–380.

1094 Yang L. and Steefel C. (2008) Kaolinite dissolution and precipitation kinetics at 22°C and pH  
1095 4. *Geochim. Cosmochim. Acta* **72**, 99–116.

1096 Zheng X-Y., Beard B.L., and Johnson C.M. (2019) Constraining silicon isotope exchange  
1097 kinetics and fractionation between aqueous and amorphous Si at room temperature. *Geochim.*  
1098 *Cosmochim. Acta* **253**, 267–289.

1099 Zhu C., Rimstidt J.D., Zhang Y.L., Kang J.T., Schott J., and Yuan H.L. (2020) Decoupling  
1100 feldspar dissolution and precipitation rates at near-equilibrium with Si isotope tracers:  
1101 Implications for modeling silicate weathering. *Geochim. Cosmochim. Acta* **271**, 132–153.

1102 Ziegler K., Chadwick O. A., Brzewinski M. A. and Kelly E. F. (2005a) Natural variations of  
1103  $\delta^{30}\text{Si}$  ratios during progressive basalt weathering, Hawaiian Islands. *Geochim. Cosmochim.*  
1104 *Acta* **69**, 4597–461.

1105 Ziegler K., Chadwick O.A., White A. F. and Brzezinski M. A. (2005b)  $\delta^{30}\text{Si}$  systematics in a  
1106 granitic saprolite, Puerto Rico. *Geology* **33**, 817–820.

1107  
1108  
1109  
1110  
1111  
1112  
1113  
1114  
1115  
1116  
1117

1118 **FIGURE CAPTIONS**

1119  
1120 **Figure 1.** Dissolved silica concentration timeseries for the high (red circles), medium (green  
1121 diamonds), and low (blue squares) surface area batch experiments (**A**) from Fernandez et al.  
1122 (2019) and (**B**) corresponding measured fluid  $\delta^{30}\text{Si}$  (open markers, Fernandez et al., 2019)  
1123 and Ge/Si ratios (solid markers, this study) as a function of time for the ~30-day experiments.  
1124 Error bars correspond to 2 standard deviations for the Si stable isotope measurements. Ge/Si  
1125 analytical uncertainty is within the marker sizes and correspond to 2% and 5% RSD for Ge  
1126 and Si concentration measurements, respectively. Initial Ge/Si composition of the bulk phase  
1127 is represented by the grey bar and red, green, and blue lines correspond to the evolving Ge/Si  
1128 amorphous silica composition with time (see **Table 2**). Fluid Ge/Si ratios remain elevated  
1129 with respect to the compositions of the high ( $0.28 \pm 0.01 \mu\text{mol mol}^{-1}$ ), medium ( $0.56 \pm 0.02$   
1130  $\mu\text{mol mol}^{-1}$ ), and low ( $0.64 \pm 0.02 \mu\text{mol mol}^{-1}$ ) surface area seed crystals.

1131 **Figure 2.** Fluid  $\delta^{30}\text{Si}$  as a function of Ge/Si ratio for the high (red circles), medium (green  
1132 diamonds), and low (blue squares) surface area batches. Starting values are the points on the  
1133 far left of the graph. A parabolic-type relationship characterizes the  $\delta^{30}\text{Si}$  and Ge/Si variability  
1134 in the high surface area batch, which represents fast  $\delta^{30}\text{Si}$  re-equilibration relative to the rates  
1135 of Ge/Si equilibrium partitioning (that are negligible over this experimental timespan). Error  
1136 bars represent 2 standard deviation for the Si stable isotope data (Fernandez et al. 2019) and  
1137 2% and 5% RSD for Ge and Si concentration measurements used in Ge/Si calculations.

1138 **Figure 3.** Fluid silicon (**A**) and germanium (**B**) concentrations as a function of the  
1139 experimental duration (~35 days). Ge kinetic rate constant ( $\log k_{f,\text{Ge}}$ ) was determined based  
1140 on a “best-fit” approach of the three mass exchange models (**section 4.2**) to the experimental  
1141 data for a given Ge equilibrium constant ( ${}^{\text{Ge}}K_{\text{eq}} = 10^{-3.8198}$ ) calculated based on an equilibrium  
1142 thermodynamic model assuming ideal solid–state solution (Eq. 3) between quartz ( $\text{SiO}_2$ ) and  
1143 argutite ( $\text{GeO}_2$ ). The range of Ge kinetic rate constants tested spanned roughly 7 orders of

1144 magnitude from  $10^{-12.6}$  to  $10^{-19.8}$  mol m<sup>-2</sup> s<sup>-1</sup>. Errors are 2% and 5% RSD for Ge and Si  
1145 concentration measurements used in Ge/Si calculations.

1146 **Figure 4.** Trace model simulations of fluid Ge/Si over the duration of the amorphous silica  
1147 precipitation experiments across all surface areas for the three “**no back reaction**”, “**bulk**”,  
1148 and “**surface**” mass exchange scenarios (A). Fluid Ge/Si simulations are compared to  
1149 previous simulations performed across the same exchange scenarios for fluid  $\delta^{30}\text{Si}$  (B)  
1150 reported in **Fernandez et al. (2019)**. Fluid  $\delta^{30}\text{Si}$  show higher sensitivity to the different  
1151 approaches in which the fluid can interact with the growing amorphous silica phase. The  
1152 “**surface**” approach provides the best fit to the high surface area Ge/Si and  $\delta^{30}\text{Si}$ . However,  
1153 the time intervals (or fluid–mineral interaction depths) determined based on sensitivity  
1154 analyses for Ge/Si and  $\delta^{30}\text{Si}$  are distinct, > 14 days (C) and 1 day (D), respectively. Error bars  
1155 correspond to  $\pm 2$  SD for Si stable isotopes (C, D). Analytical uncertainty for Ge/Si  
1156 measurements correspond to 1–3% RSD and are within the bounds of the symbols.

1157 **Figure 5.** Long-term model simulations for the evolution of the observed Ge partition  
1158 coefficient,  $K_D$ , over 1000 years for the high (A), medium (B), and low (C) surface area  
1159 conditions. Predictions from the two different fluid–mineral equilibration scenarios; “**bulk**”  
1160 (dashed line) and “**surface**” (solid line) are shown alongside the predicted equilibrium  
1161 partition coefficient,  $K_D^{\text{EQ}}$ , equal to 12.8 (Eq. 3). In all cases, observed  $K_D$  behavior suggest  
1162 that Ge partitioning is still far from equilibrium conditions at the end of the simulation.

1163 **Figure 6.** Instantaneous partition coefficient,  $K_D^{\text{inst}}$ , as a function of experimentally  
1164 determined silica precipitation rates (presented here in log units; Fernandez et al., 2019) for  
1165 the high (A), medium (B), and low (C) surface area amorphous silica precipitation batch  
1166 experiments. The different  $K_D$  trends represent different methods of calculating the partition  
1167 coefficient. To account for the evolving bulk amorphous silica composition with time in  
1168 these “free-drifting” experiments,  $K_D^{\text{inst}}$  can be calculated either through the traditional

1169 method (Eq. 4a) or through a modified Rayleigh distillation approach (Eq. 4b, Tang et al.,  
1170 2008).

1171 **Figure 7.** Normalized  $K_D^{\text{inst}}$  ( $K_D^*$ ,  $\text{Ge/Si}_{\text{fluid}} = \text{Ge/Si}_{\text{solid}}$ ) as a function of silica precipitation  
1172 rates ( $\log R_p$ ) for long term simulations (1000 years).  $K_D^*$  can be calculated using the “bulk”  
1173 or total solid (**A**) or cumulatively precipitated (**B**) composition. The predicted instantaneous  
1174 partition coefficient at equilibrium,  $K_D$  equal to  $\sim 12.8$  (Eq. 3), is represented by a yellow star.  
1175 High, medium, and low surface area experimental data ( $\sim 35$  days) are shown as solid  
1176 markers whereas numerical predictions are depicted as shaded gray areas. Mass balance and  
1177 model predictions performed using the “surface” fluid-mineral mass exchange scenario are  
1178 parsed out for each given surface area (**C**). At early times,  $K_D^*$  is observed to decrease with  
1179 decreasing precipitation rates as a result of quasi-conservative Ge behavior during the  
1180 beginning of amorphous silica growth. At (near) equilibrium conditions, the relationship  
1181 between  $K_D$  and  $R_p$  flips from a positive to an inverse correlation where  $K_D$  increases with  
1182 decreasing  $R_p$ .

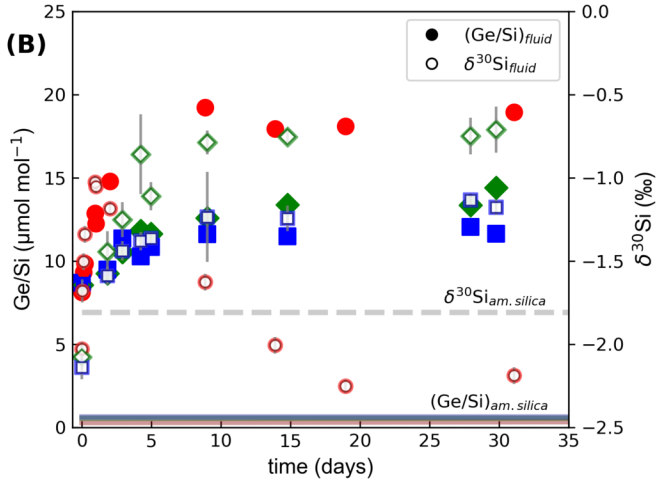
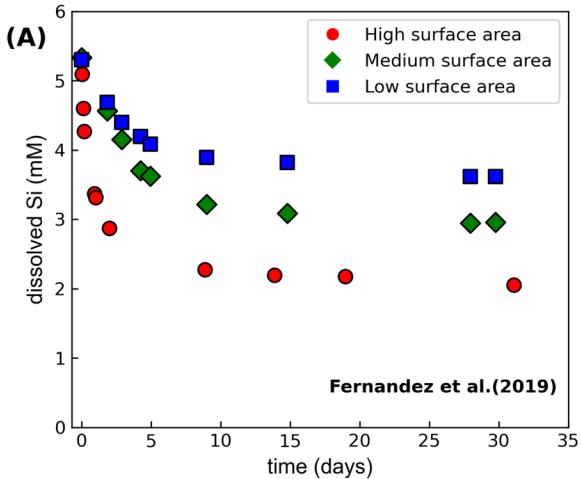
1183 **Figure 8.** Measured  $\delta^{30}\text{Si}_{\text{fluid}}$  as a function of  $(\text{Ge/Si})_{\text{fluid}}$  for the surface area batch  
1184 experiments (depicted as markers) presented alongside trace model predictions for the  
1185 respective surface area conditions over longer timescales, from 6 months to 20 years.  
1186 Predicted equilibrium  $\delta^{30}\text{Si}_{\text{fluid}}$  and  $(\text{Ge/Si})_{\text{fluid}}$  are represented by a yellow star, corresponding  
1187 to values of  $-2.73 \pm 0.07 \text{‰}$ , calculated from the measured starting  $\delta^{30}\text{Si}_{\text{fluid}}$  (Fernandez et al.  
1188 2019) and experimentally constrained equilibrium fractionation factor (Stamm et al., 2019),  
1189 and  $\sim 0.02 - 0.05 \mu\text{mol mol}^{-1}$ , respectively.

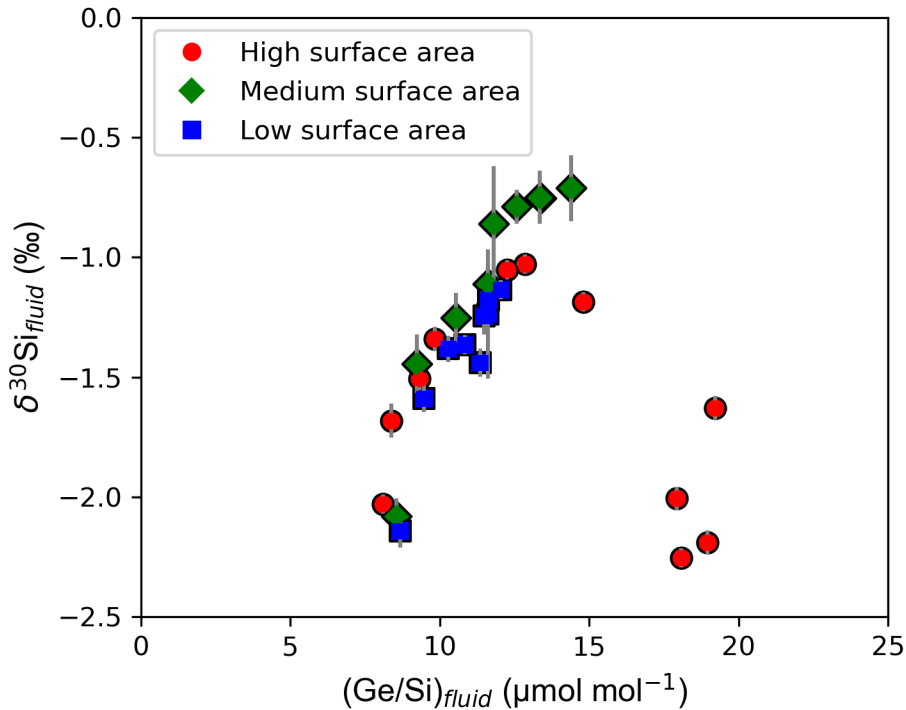
1190 **Figure 9.** Calculated observed Si stable isotope fractionation factors,  $\Delta_{\text{cumul.ppt-fluid}}$ , as a  
1191 function of the normalized instantaneous Ge partition coefficient,  $K_D^*$  (i.e.  $(\text{Ge/Si})_{\text{fluid}} =$   
1192  $(\text{Ge/Si})_{\text{am.silica}}$ ), using the composition of the cumulative precipitate as a function of time  
1193  $((\text{Ge/Si})_{\text{ppt}})$ . All surface area batch experiments (depicted as markers) are presented alongside

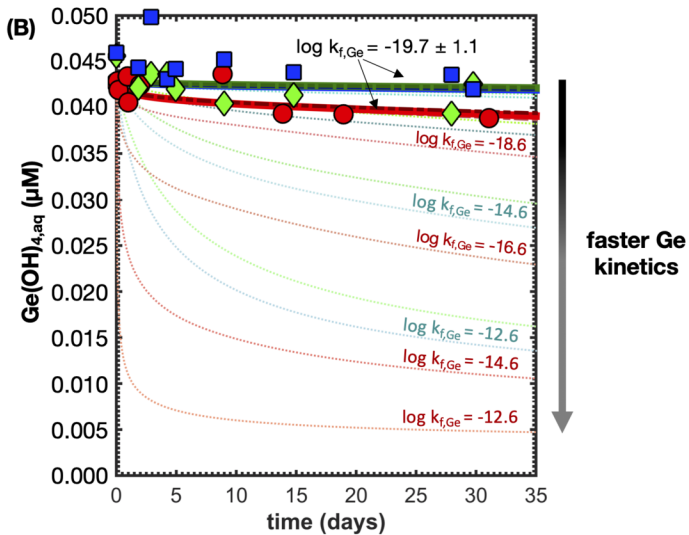
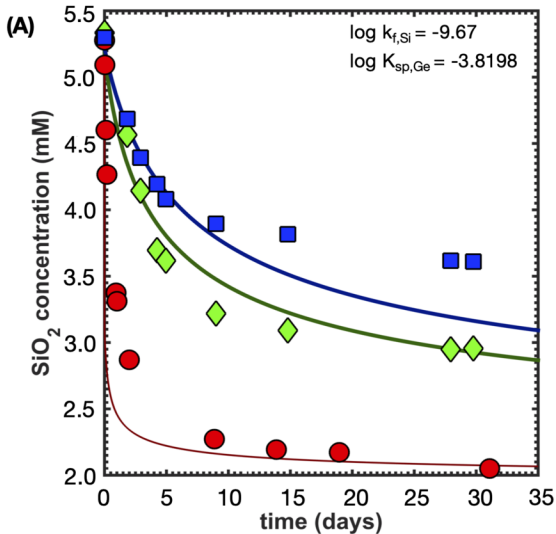
1194 trace model fluid  $\Delta_{\text{cumul.ppt-fluid}}$  and  $K_D^{\text{inst}}$  predictions from the “**surface**” simulation (with a  
1195 time interval > 14 days) from 6 months to 20 years. The equilibrium fractionation factor  
1196 ( $^{30/28}\Delta_{\text{EQ(am.silica-fluid)}}$ ) and partition coefficient ( $D_{\text{EQ}}$ ) for amorphous silica derives from Stamm  
1197 et al. (2019) and this study (Eq. 3), respectively. At 20 years,  $\Delta_{\text{cumul.ppt-fluid}}$  values suggest that  
1198 Si stable isotopes are very close to equilibrium in the high surface area case whereas observed  
1199  $K_D^*$  values at the end of the simulation show that the system is still far from equilibrium for  
1200 Ge. These results further highlight the distinct equilibration timescales between Ge/Si and  
1201  $\delta^{30}\text{Si}$ .

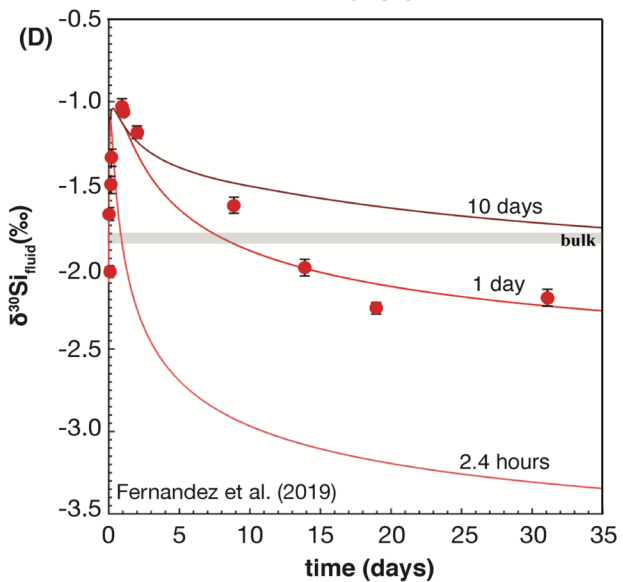
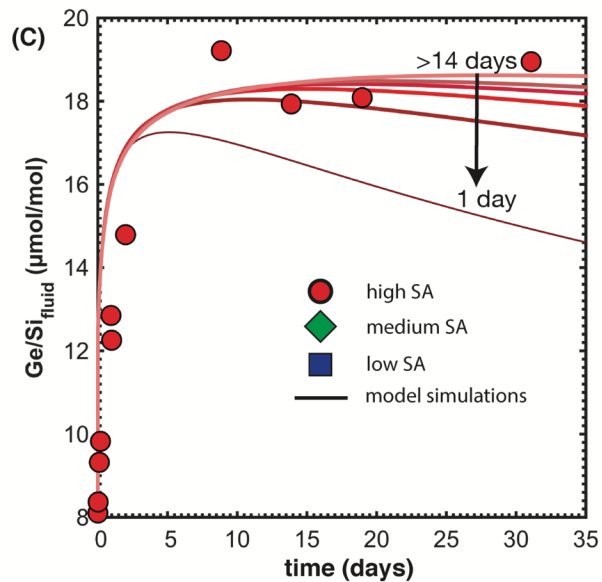
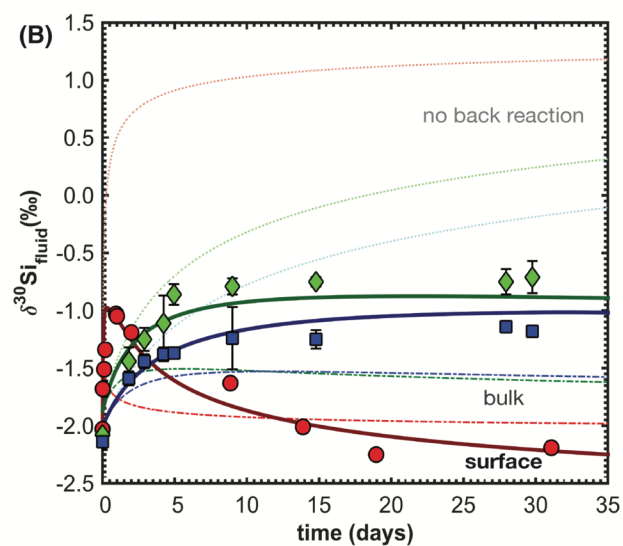
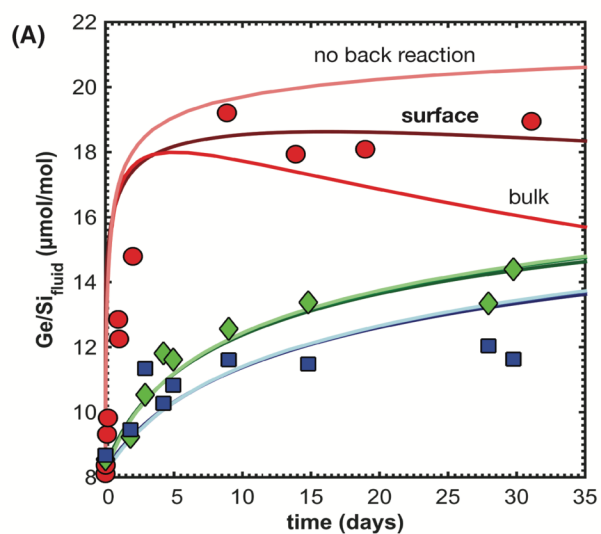
1202

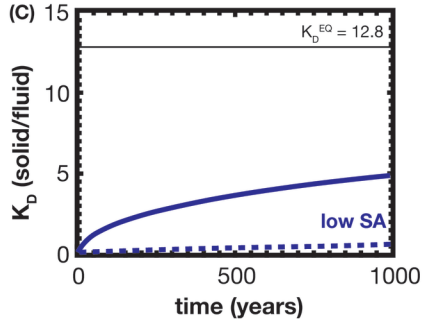
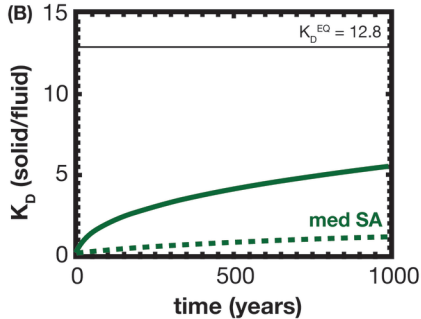
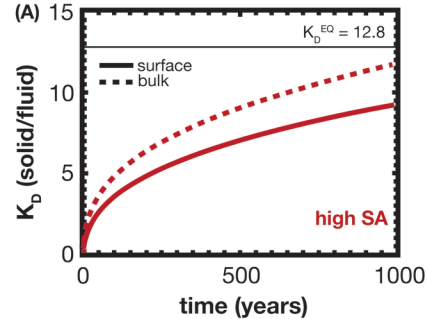
1203

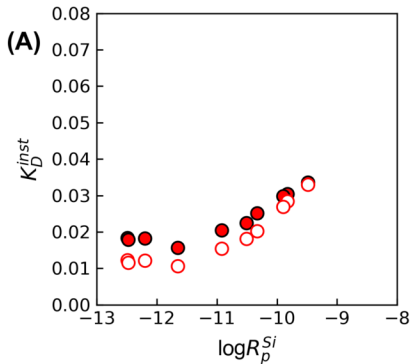






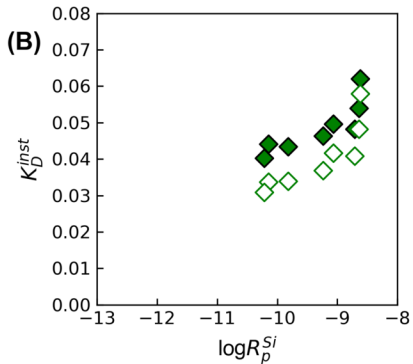






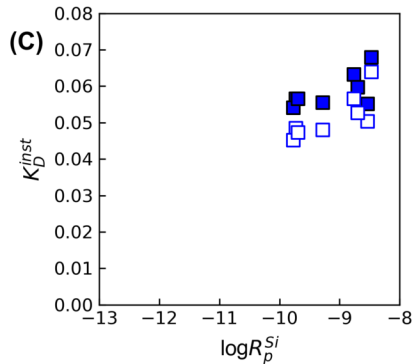
High surface area

- $K_D^{inst}$  (traditional, Eq. 5a)
- $K_D^{inst}$  (Rayleigh, Eq. 5b)



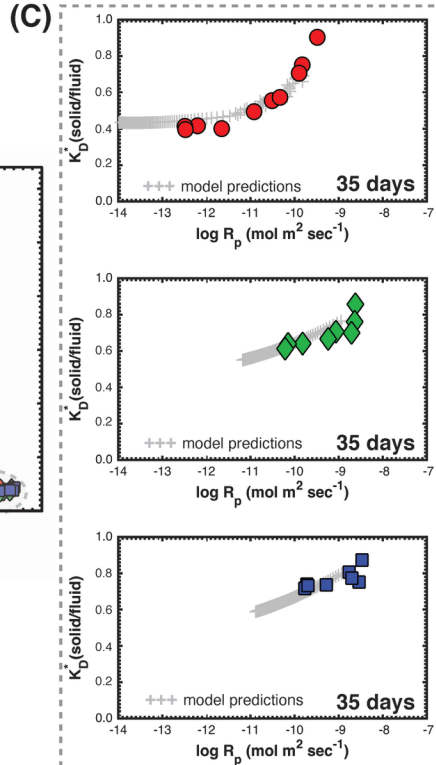
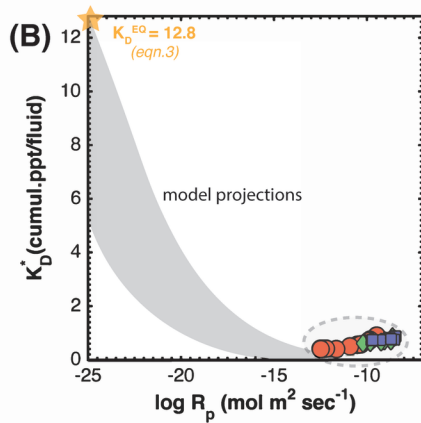
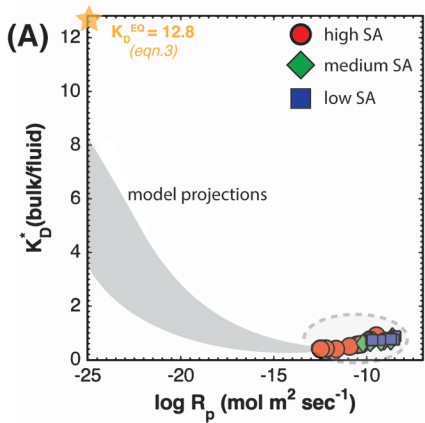
Medium surface area

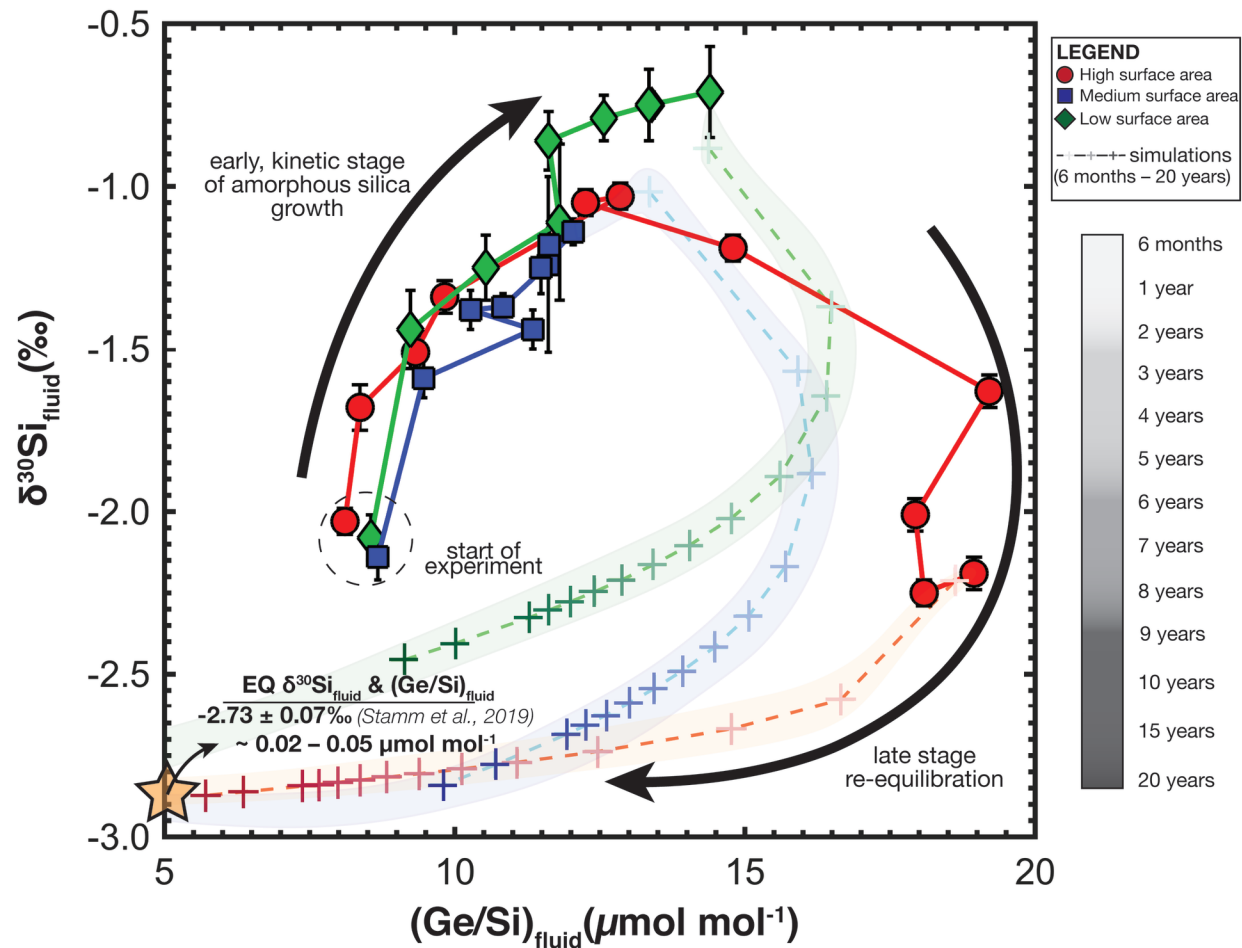
- ◆  $K_D^{inst}$  (traditional, Eq. 5a)
- ◇  $K_D^{inst}$  (Rayleigh, Eq. 5b)



Low surface area

- $K_D^{inst}$  (traditional, Eq. 5a)
- $K_D^{inst}$  (Rayleigh, Eq. 5b)





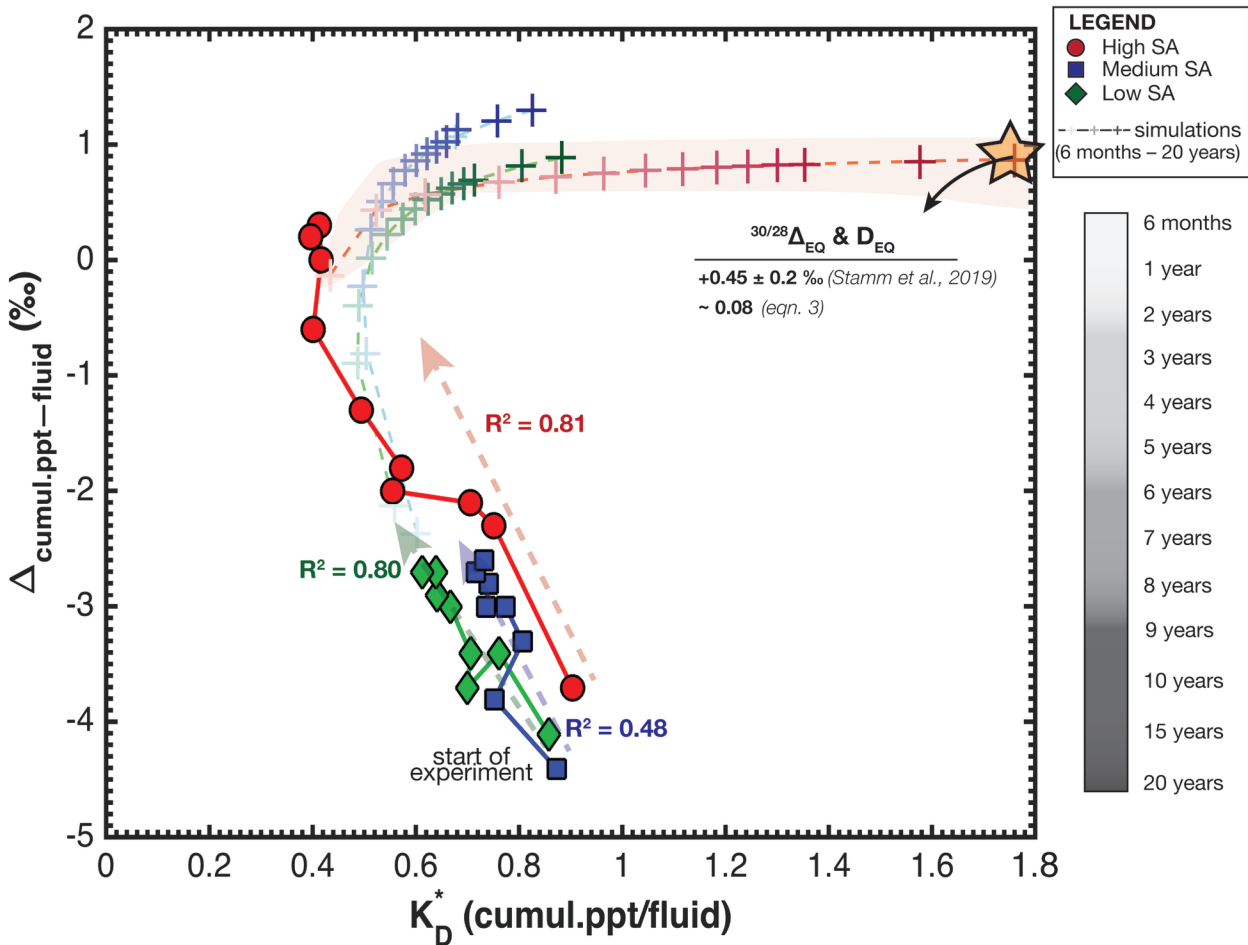


**Table 1.** Starting conditions for all three amorphous silica precipitation batch experiments

<b>Physical parameters</b>	<b>High SA</b>	<b>Med SA</b>	<b>Low SA</b>
<b>SiO<sub>2(aq)</sub> [mM]<sup>*</sup></b>	5.3 ± 0.7	5.3 ± 0.4	5.3 ± 0.5
<b>Ge(OH)<sub>4</sub> [μM]<sup>‡</sup></b>	0.043 ± 0.001	0.044 ± 0.001	0.046 ± 0.001
<b>Ω [log Q/K]<sup>¥</sup></b>	-3.95	-3.95	-3.95
<b>GeOH<sub>4(aq)</sub> [μg]<sup>‡</sup></b>	0.157 ± 0.003	0.80 ± 0.02	0.83 ± 0.02
<b>GeO<sub>2(s)</sub> [μg]</b>	0.166 ± 0.003	2.90 ± 0.06	3.35 ± 0.07
<b>GeO<sub>2(s)</sub> : GeOH<sub>4(aq)</sub> [μg/μg]<sup>†</sup></b>	1.06 ± 0.03	3.6 ± 0.1	4.0 ± 0.1
<b>S [m<sup>2</sup>]<sup>*</sup></b>	25 ± 8	0.54 ± 0.02	0.31 ± 0.02

\* Fernandez et al. (2019)

‡ Measured fluid Ge concentrations with an analytical uncertainty of 2% RSD.

¥ Saturation states for GeO<sub>2</sub> calculated using CrunchTope

† solid to fluid mass ratio calculated as the initial amount of Ge present in both the amorphous silica seed and fluid phase (GeOH<sub>4</sub>). Error calculated based on standard error propagation using 2% RSD analytical uncertainty for Ge concentrations measurements.

**Table 2. Germanium data for amorphous silica precipitation experiments**

No.	time days	Si(OH) <sub>4</sub> <sup>(a)</sup>	Ge(OH) <sub>4</sub> <sup>(b)</sup>	N <sub>GeO2(ppt)</sub> <sup>(c)</sup>	N <sub>GeO2(am.silica)</sub> <sup>(d)</sup>	log R <sub>p</sub> <sup>Si (a)</sup>	log R <sub>p</sub> <sup>Ge (e)</sup>	(Ge/Si) <sub>fluid</sub> <sup>f</sup>	(Ge/Si) <sub>ppt</sub> <sup>g</sup>	(Ge/Si) <sub>am.silica</sub> <sup>h</sup>	K <sub>D</sub> <sup>inst (i)</sup>
		μM	pM	pmoles		mole m <sup>-2</sup> s <sup>-1</sup>		μmol/mol		bulk/fluid	
<i>High surface area batch (50 m<sup>2</sup> g<sup>-1</sup>)</i>											
1	0.00	5277 ± 700	42776 ± 856		2291 ± 46			8.11 ± 0.13		0.28 ± 0.09	0.035 ± 0.006
2	0.02	5092 ± 500	42599 ± 852	52 ± 1207	2343 ± 1208	-9.48 ± 0.5	-14.9 ± 1.4	8.37 ± 0.10	2 ± 23	0.28 ± 0.52	0.034 ± 0.018
3	0.11	4600 ± 600	42855 ± 858	80 ± 1211	2371 ± 1711	-9.82 ± 0.1	-15.5 ± 1.2	9.32 ± 0.13	1 ± 15	0.28 ± 0.72	0.031 ± 0.022
4	0.19	4266 ± 700	41908 ± 838	169 ± 1199	2461 ± 2089	-9.90 ± 0.4	-15.4 ± 0.9	9.82 ± 0.16	2 ± 7	0.29 ± 0.85	0.032 ± 0.028
5	0.93	3375 ± 900	43382 ± 868	143 ± 1206	2434 ± 2413	-10.51 ± 0.5	-16.1 ± 0.9	12.85 ± 0.27	1 ± 8	0.29 ± 1	0.024 ± 0.029
6	1.00	3311 ± 100	40579 ± 812	314 ± 1188	2605 ± 2689	-10.33 ± 0.6	-15.8 ± 0.6	12.25 ± 0.04	2 ± 4	0.31 ± 1.03	0.026 ± 0.027
7	2.00	2870 ± 600	42451 ± 849	271 ± 1175	2562 ± 2935	-10.92 ± 0.7	-16.1 ± 0.6	14.79 ± 0.21	2 ± 4	0.30 ± 1.15	0.022 ± 0.027
8	8.87	2272 ± 200	43638 ± 873	262 ± 1218	2553 ± 3177	-11.65 ± 0.7	-16.8 ± 0.7	19.21 ± 0.09	1 ± 4	0.30 ± 1.25	0.015 ± 0.020
9	13.88	2193 ± 500	39336 ± 787	488 ± 1175	2779 ± 3387	-12.20 ± 0.7	-16.7 ± 0.4	17.93 ± 0.23	3 ± 2	0.33 ± 1.22	0.020 ± 0.025
10	18.95	2172 ± 400	39278 ± 786	530 ± 1112	2821 ± 3565	-12.49 ± 0.6	-16.8 ± 0.3	18.08 ± 0.18	3 ± 2	0.33 ± 1.26	0.019 ± 0.025
11	31.08	2051 ± 400	38855 ± 777	586 ± 1105	2877 ± 3733	-12.47 ± 0.7	-17.0 ± 0.3	18.95 ± 0.20	3 ± 2	0.34 ± 1.30	0.018 ± 0.025
	seed <sub>init</sub>									0.28 ± 0.01	
	seed <sub>final</sub>									0.33 ± 0.02	
<i>Medium surface area batch (0.127 m<sup>2</sup> g<sup>-1</sup>)</i>											
1	0.00	5334 ± 400	45631 ± 879		39982 ± 800			8.55 ± 0.08		0.56 ± 0.02	0.066 ± 0.005
2	1.83	4565 ± 400	42161 ± 843	994 ± 1243	40976 ± 1478	-8.62 ± 0.5	-13.9 ± 0.1	9.24 ± 0.09	5 ± 1	0.57 ± 0.04	0.063 ± 0.006
3	2.90	4144 ± 800	43658 ± 873	755 ± 1214	40737 ± 1912	-8.63 ± 0.6	-14.2 ± 0.2	10.53 ± 0.19	2 ± 2	0.57 ± 0.05	0.056 ± 0.013
4	4.23	3696 ± 500	43641 ± 873	890 ± 1235	40872 ± 2276	-8.70 ± 0.9	-14.3 ± 0.1	11.81 ± 0.14	2 ± 1	0.57 ± 0.06	0.049 ± 0.008
5	4.95	3618 ± 500	42024 ± 840	1406 ± 1212	41388 ± 2579	-9.04 ± 0.6	-14.2 ± 0.1	11.62 ± 0.14	3 ± 1	0.58 ± 0.06	0.051 ± 0.008
6	9.00	3219 ± 400	40454 ± 809	1901 ± 1167	41883 ± 2579	-9.23 ± 0.8	-14.3 ± 0.2	12.57 ± 0.13	3.2 ± 0.7	0.58 ± 0.07	0.048 ± 0.007
7	14.79	3091 ± 700	41350 ± 827	1815 ± 1157	41797 ± 3058	-9.80 ± 1.1	-14.6 ± 0.2	13.38 ± 0.23	2.9 ± 0.7	0.58 ± 0.07	0.046 ± 0.012
8	27.95	2948 ± 600	39346 ± 787	2397 ± 1142	42380 ± 3264	-10.13 ± 1.1	-14.7 ± 0.3	13.35 ± 0.20	3.6 ± 0.5	0.59 ± 0.08	0.046 ± 0.012
9	30.00	2955 ± 500	42548 ± 851	1792 ± 1159	41774 ± 3463	-10.09 ± 0.9	-14.8 ± 0.2	14.40 ± 0.17	2.6 ± 0.7	0.58 ± 0.08	0.042 ± 0.009
	seed									0.56 ± 0.02	
<i>Low surface area batch (0.072 m<sup>2</sup> g<sup>-1</sup>)</i>											
1	0.00	5298 ± 500	45957 ± 919		46054 ± 921			8.7 ± 0.1		0.64 ± 0.02	0.074 ± 0.008
2	1.83	4686 ± 500	44345 ± 887	514 ± 1277	46567 ± 1575	-8.47 ± 0.2	-14.0 ± 0.4	9.46 ± 0.11	3 ± 3	0.64 ± 0.03	0.069 ± 0.008
3	2.90	4394 ± 400	49849 ± 997	-724 ± 1334	45330 ± 2064	-8.54 ± 0.3		11.34 ± 0.09	-2 ± 2	0.62 ± 0.05	0.056 ± 0.006
4	4.23	4194 ± 600	43084 ± 862	1042 ± 1318	47095 ± 2449	-8.76 ± 0.6	-14.0 ± 0.1	10.27 ± 0.14	3 ± 1	0.65 ± 0.05	0.065 ± 0.011
5	4.95	4080 ± 300	44194 ± 884	883 ± 1234	46936 ± 2742	-8.70 ± 0.5	-14.2 ± 0.1	10.83 ± 0.08	2 ± 1	0.65 ± 0.06	0.060 ± 0.006
6	9.00	3895 ± 300	45226 ± 905	748 ± 1265	46802 ± 3020	-9.28 ± 0.7	-14.5 ± 0.2	11.61 ± 0.08	2 ± 2	0.64 ± 0.06	0.056 ± 0.006
7	14.79	3817 ± 400	43839 ± 877	1187 ± 1260	47241 ± 3272	-9.72 ± 1.1	-14.49 ± 0.03	11.48 ± 0.11	3 ± 1	0.65 ± 0.07	0.057 ± 0.007
8	27.95	3618 ± 500	43555 ± 871	1363 ± 1236	47416 ± 3498	-9.77 ± 1.1	-14.71 ± 0.04	12.04 ± 0.14	2.8 ± 0.9	0.65 ± 0.07	0.055 ± 0.009
9	30.00	3610 ± 700	41984 ± 840	1833 ± 1210	47887 ± 3701	-9.70 ± 0.9	-14.6 ± 0.2	11.63 ± 0.19	3.7 ± 0.7	0.66 ± 0.08	0.059 ± 0.013

---

seed

0.64 ± 0.02

---

- a. Additional details on dissolved silica concentrations, saturation states, precipitation rates, evolving surface area, and Si stable isotope ratios can be found in Fernandez et al. (2019)
- b. Measured fluid Ge concentrations with associated errors of ± 2% RSD.
- c. Cumulative mass of amorphous GeO<sub>2</sub> precipitated out of solution. Values determined by subtracting the picomoles Ge in solution at time, t, from initial amount in solution, at t=0.
- d. Total mass amorphous silica present in the system with associated errors calculated using error propagation.
- e. Time-averaged precipitation rates for GeO<sub>2</sub> normalized to the surface area:  $R_p^{Ge} = \frac{N_{GeO_2(pppt)_{t_I}} - N_{GeO_2(pppt)_{t_{II}}}}{S \cdot \Delta t_{II-I}}$  (see **eqn.5** in **Fernandez et al., 2019** for further details). Uncertainty determined via standard error propagation.
- f. Measured fluid Ge/Si ratios where uncertainty determined using error propagation of the analytical uncertainties for Si (± 5% RSD) and Ge (± 2% RSD), respectively.
- g. Ge/Si ratios of the cumulatively precipitated amorphous silica. Determined through mass balance calculations using the cumulative mass of amorphous GeO<sub>2</sub> removed ( $N_{GeO_2(pppt)}$ ) and SiO<sub>2</sub> ( $N_{SiO_2(pppt)}$  ; **Table 2 in Fernandez et al., 2019**). Uncertainty calculated using standard error propagation according to sum of squares.
- h. Amorphous silica Ge/Si ratios were estimated by tracking the total amount of GeO<sub>2</sub> and SiO<sub>2</sub> accumulating in the growing bulk ( $n_{Ge,SiO_2, bulk(t=0)} + n_{Ge,SiO_2, cumulative(t)}$ ). Uncertainty calculated via error propagation according to the sum of squares using both the analytical error for the initial seeds and measured fluid Ge and Si uncertainties.
- i. The instantaneous partition coefficient calculated as  $\frac{(Ge/Si)_{am.silica}}{(Ge/Si)_{fluid}}$ , monitored throughout the course of the reaction for an evolving bulk solid phase.
- j. Normalized instantaneous partition coefficients for an initial Ge/Si<sub>fluid</sub> ratio equal to Ge/Si<sub>solid</sub> and error calculated using Monte Carlo.

**Table 3. Initial conditions for the Ge, trace element batch model**

Parameters	units	conservative	Ge incorporation
reaction order		3.5	3.5
duration		35 days	35 days 1 to 1000 years
timestep	hours	9.6	9.6
T	°C	25	25
pH		7.33	7.33
Specific surface area	m <sup>2</sup> g <sup>-1</sup>	50	50
		0.127	0.127
		0.072	0.072
Si(OH) <sub>4(aq)</sub> <sup>a</sup>	mM	5.277	5.277
Ge(OH) <sub>4(aq)</sub> <sup>b</sup>	mM	4.2776 x 10 <sup>-5</sup>	4.2776 x 10 <sup>-5</sup>
log k <sub>f(SiO2)</sub> <sup>c</sup>		-9.67	-9.67
log k <sub>f(GeO2)</sub> <sup>d</sup>		-	-19.7
log K <sub>eq(SiO2)</sub> <sup>e</sup>		-2.7135	-2.7135
log K <sub>eq(GeO2)</sub> <sup>f</sup>		-	-3.8198
(Ge/Si) <sub>fluid</sub>	μmol mol <sup>-1</sup>	8.11	8.11
		0.28 (high)	0.28 (high)
(Ge/Si) <sub>am.silica</sub>	μmol mol <sup>-1</sup>	0.56 (medium)	0.56 (medium)
		0.64 (low)	0.64 (low)
D <sub>EQ</sub> <sup>g</sup>		-	0.08
D <sub>kin</sub> <sup>h</sup>		-	9.3 × 10 <sup>-11</sup>

a. Measured starting dissolved Si concentrations from Fernandez et al. (2019).

b. Measured starting dissolved Ge concentrations from this study.

c. Rimstidt and Barnes (1980)

d. Determined through taking a best fit of the experimental fluid Ge/Si data.

e. Gunnarsson and Anórrsson (2000)

f. Estimated using Evans and Derry (2002) equilibrium model for germanium bearing quartz (**Section 2.3, Eq. 3**).

g. Equilibrium partition coefficient (D<sub>EQ</sub>) calculated as the ratio between GeO<sub>2(am)</sub> and SiO<sub>2(am)</sub> equilibrium constants,  $\frac{K_{eq,GeO_2}}{K_{eq,SiO_2}}$ .

h. Kinetic partition coefficient calculated as the ratio between GeO<sub>2(am)</sub> and SiO<sub>2(am)</sub> precipitation rate constants:  $\frac{k_{f,GeO_2}}{k_{f,SiO_2}}$ .